

POLITECNICO DI TORINO

Master of Science in Automotive Engineering



Master's Degree Thesis

Re-design in AlSi10Mg alloy of an ICE piston for SLM process

Supervisor:

Prof. Andrea Tridello

Candidate:

Isabel Trinchieri

McMaster University supervisor:

Prof. Mo Elbestawi

Academic Year: 2022/2023

POLITECNICO DI TORINO

Master of Science in Automotive Engineering



Master's Degree Thesis

Re-design in AlSi10Mg alloy of an ICE piston for SLM process

Supervisor:

Prof. Andrea Tridello

Candidate:

Isabel Trinchieri

McMaster University supervisor:

Prof. Mo Elbestawi

Academic Year: 2022/2023

To Paolo, my lovely father

Acknowledgements

I feel extremely grateful to have had the opportunity to pursue my master thesis in the Department of Mechanical Engineering at McMaster University, Canada, thanks to the collaboration between Politecnico di Torino and the STELLANTIS group. First and foremost, I would like to thank my Italian supervisor, Professor Andrea Tridello for his help and valuable suggestions, which remarkably improved my thesis work. I am grateful to him for shaping me with a critical thinking attitude, which enables me being always motivated. I gratefully thank Professor Maria Pia Cavatorta, whose contribution was essential in planning and motivating this cooperation with McMaster University. I would like to extend my gratitude to my Canadian supervisor, Mohamed Elbestawi and his team for being an example of his dedication to work and hospitality and care for the students, making me feel very welcome in the amazing country that Canada is.

Although no words in the world can ever fully express it, I must give my deep and sincere gratitude to my family, especially my parents Paolo and Nidia and my brother Lorenzo, for giving me the chance to realize my ambitions. I know you would be proud of me dad; I miss you every single second of my life. Thanks to the strongest woman I know, thanks mum for your unconditional love and support, I would not be where I am today without it.

I want also to thank my Canadian friends for their help during this hard time, especially Claire Stewart and her family for their love and support, Natasha, Tim and Paolo, naming them all is not possible but if you are reading this page, you know how special you are to me.

Last but not least I owe my deepest thanks to Simone for always being understanding and encouraging through the best and worst of times.

Abstract

The use of components produced with Additive manufacturing (AM) processes has grown significantly over the past decade, finding use in rapid prototyping, rapid manufacturing and functional end-usable products, allowing performance enhancement of lightweight parts. Selective laser melting (SLM), one of the most promising AM technologies, can be applied to build metal parts layer by layer within a powder bed system. In comparison to conventional casting, SLM enables the production of components with customizable shapes, increasing both freedom of design and material usage efficiency.

This thesis focuses on the re-design for SLM manufacturing of the piston of a four-stroke engine, originally produced with conventional processes and with AlCu4MgSi as constitutive material, with a particular focus on the selection of optimal parameters for the SLM process.

As aluminum alloys are widely used in the automotive and aerospace industries due to an exceptional combination of low density and competitive mechanical qualities, AlSi10Mg alloy powder is chosen as the material for this production. Using a design of experiment methodology based on energy density, the influence of process parameters such as scan speed, hatch spacing and laser power on the density and hardness of the final part is experimentally analyzed. The optimized process parameters are selected to maximize the relative density and subsequently used to build samples to assess their mechanical properties under tensile tests at room temperature.

Afterwards, topological optimization of the part is carried out by using the Altair Inspire software and three designs of the same piston are obtained. The final design is the one ensuring the same performance as the baseline configuration. Finally, a printing simulation of the building process is carried out in Inspire environment, considering the proper part orientation and support generation in the building chamber volume. The re-designed AM component results in an overall mass reduction of 3% with respect to the original piston designed for slush casting.

Improving productivity of AM processes remains a challenge due to the limits in build rates and volumes, processable materials and the high cost of metal powder production and of equipment. A more comprehensive understanding of the additive manufacturing and innovations are required to improve the technological efficiency of the AM processes themselves.

Table of contents

1. Introduction	1
2. Part selection	3
2.1 Load cases	4
2.2 Constraints	7
2.3 FEM analysis on the original part	8
3. AM Process configuration	12
3.1 Selective Laser Melting	12
3.2 Material selection and powder characterization	14
3.3 Process parameters optimization	17
3.3.1 Process parameters overview	18
3.3.2 Experimental analysis	22
3.3.2.1 Experimental results: densification level	23
3.3.2.2 Experimental results: microhardness	27
3.3.2.3 Experimental results: microstructural defects and meltpools	31
3.3.3 Concluding remarks	35
4. Topology optimization of the part	37
4.1 Tensile test	37
4.2 FEM analysis on the AlSi10Mg part	39
4.3 Design optimization	42
4.3.1 1st Design	44
4.3.2 2nd Design	46
4.3.3 3rd Design	48
4.4 Final design choice	50
5. Build process	52
6. Conclusions	57

Appendix	58
References	60

Nomenclature

Greek Symbols

α	Ratio of temperature expansion
ρ	Material density
ρ_d	Dry density of the sample
ρ_w	Wet density of the sample
λ	Heat conductivity
ν	Poisson ratio

Latin Symbols

E	Elastic modulus
G	Rigidity modulus
T_{sol}	Solidification temperature
T_{liq}	Melting temperature
C_p	Specific heat
TDC_f	Top dead Centre firing
DoF	Degrees of Freedom
F_n	Thrust force
F_g	Gas force
F_l	Liner reaction force
K	Global stiffness matrix
x	Displacement vector response
f	Vector of the external forces applied
SF	Safety Factor
P	Laser power
v	Scan speed
h	Hatch spacing
t	Layer thickness
E_V	Volumetric energy density
HV	Vickers Hardness
$F_{(gf)}$	Load expressed in grams-force

$d_{V(\mu m)}$	Indentation diagonal in micrometers
Q	Heat input
YS	Yield stress
UTS	Ultimate Tensile Strength
w	Whisker's multiplier
q_1	25 th percentiles of the sample data
q_3	75 th percentiles of the sample data

List of figures

Figure 1 CAD model of the baseline piston (isometric and internal views).....	3
Figure 2 Piston drawing with main quotations in mm.....	4
Figure 3 Forces exerted on the piston.....	5
Figure 4 Trend of the thrust force during the engine cycle.....	5
Figure 5 Variation of inertia force with crank angle [1]	6
Figure 6 Variation of gas force with crank angle [1]	6
Figure 7 Variation of piston acceleration with crank angle [1].....	7
Figure 8 Piston constraints.....	8
Figure 9 Factor of Safety - Baseline piston in AlCu4MgSi.....	10
Figure 10 Von Mises Stress - Baseline piston in AlCu4MgSi	10
Figure 11 Tension/Compression Stress - Baseline piston in AlCu4MgSi.....	11
Figure 12 SLM process. (i) High-power laser melts selective areas of the powder bed. (ii) Process is repeated for successive layers. (iii) Loose powder [3].....	13
Figure 13 The effect of alloying elements on the relative crack sensitivity of aluminum alloys [4]	14
Figure 14 Al-Si phase diagram [5]	15
Figure 15 SLM process parameters: laser power, scanning speed, hatch spacing and layer thickness [3]	18
Figure 16 Schematic representation of efficient process, insufficient penetration and keyhole effect [8]	19
Figure 17 Processing map for SLM of AlSi10Mg, based on the top view of single-track scan [9]	20
Figure 18 Scanning strategy	21
Figure 19 AlSi10Mg cubes before and after sample preparation.....	22
Figure 20 Weighing support for specimens in water and in air	23
Figure 21 Relative density of AlSi10Mg parts as a function of the scan speed	24
Figure 22 Relative density vs laser power	25
Figure 23 Relative density depending on hatch spacing.....	25
Figure 24 Relative density vs volumetric energy density	26
Figure 25 HV depending on scanning speed	28
Figure 26 Vickers hardness depending on Laser Power	29

Figure 27 Vickers hardness depending on hatch spacing.....	30
Figure 28 Vickers hardness depending on Volumetric energy density.....	30
Figure 29 Relative density depending on Vickers hardness.....	31
Figure 30 Microstructure of the as-built AlSi10Mg T sample.....	32
Figure 31 Microstructure of the as-built AlSi10Mg J sample.....	32
Figure 32 Relative density depending on volumetric energy with optical microscopy images	33
Figure 33 Melt pools, magnified view sample P.....	34
Figure 34 Melt pools schematic illustration [18] left side, experimental of sample J right side	34
Figure 35 Melt pools of sample Q left side and R right side.....	35
Figure 36 Rectangular Tension Test Specimen, quotations in mm.....	37
Figure 37 Tensile tests on dogbone specimens: stress-strain curves.....	38
Figure 38 Yield stress evaluation - Test sample 5.....	38
Figure 39 Factor of Safety - Baseline piston in AlSi10Mg.....	40
Figure 40 Von Mises Stress - Baseline piston in AlSi10Mg.....	41
Figure 41 Tension/Compression Stress - Baseline piston in AlSi10Mg.....	41
Figure 42 Design and non-design space of the baseline configuration.....	42
Figure 43 Topology optimization of the part.....	43
Figure 44 From left to right: 1 st Design, 2 nd Design and 3 rd Design proposed.....	43
Figure 45 1 st Design.....	44
Figure 46 Factor of Safety - 1 st Design in AlSi10Mg.....	45
Figure 47 Von Mises Stress - 1 st Design in AlSi10Mg.....	45
Figure 48 Tension/Compression Stress - 1 st Design in AlSi10Mg.....	46
Figure 49 2 nd Design.....	46
Figure 50 Factor of Safety - 2 nd Design in AlSi10Mg.....	47
Figure 51 Von Mises Stress - 2 nd Design in AlSi10Mg.....	47
Figure 52 Tension/Compression Stress - 2 nd Design in AlSi10Mg.....	48
Figure 53 3 rd Design.....	48
Figure 54 Factor of Safety - 3 rd Design in AlSi10Mg.....	49
Figure 55 Von Mises Stress - 3 rd Design in AlSi10Mg.....	49
Figure 56 Tension/Compression Stress - 3 rd Design in AlSi10Mg.....	50
Figure 57 AM workflow for part production.....	52

Figure 58 Building platform placing of the part with supports	53
Figure 59 Building platform placing of the part with supports without rings.....	54
Figure 60 Slicing, schematic representation	54
Figure 61 Displacements during the printing phase.....	55
Figure 62 Temperature during printing phase: a) 54.4% and b) 100%	56
Figure 63 Hardness boxplots.....	59

List of tables

Table 1 AlCu4MgSi Chemical composition.....	8
Table 2 AlCu4MgSi - Mechanical properties.....	9
Table 3 AlSi10Mg Chemical composition.....	15
Table 4 AlSi10Mg powder characterization	16
Table 5 SLM process parameters applied for fabricating AlSi10Mg samples	20
Table 6 Samples density measurements.....	24
Table 7 Vickers Hardness measurements	28
Table 8 Final process parameters selection	36
Table 9 Results from tensile test data analysis.....	39
Table 10 AlSi10Mg - Mechanical properties.....	39
Table 11 FE analysis: Comparison of proposed designs.....	50
Table 12 Complete density measurements.....	58
Table 13 Complete Vickers hardness measurements.....	58

1. Introduction

The term Additive Manufacturing (AM) refers to a family of manufacturing processes considered among the most important rising technologies in the last decades, and it is developing more and more in the industrial field. The main difference from traditional technologies (subtractive processes) is that the part is built layer by layer and each successive layer is linked to the preceding one with different techniques, depending on the different AM process.

This technology allows to manufacture geometrically complex structures that can hardly be traditional processed. For this reason, it is commonly used to produce a few quality, geometrically distinctive, customizable and high value-added components, not surprisingly, leading industries include automotive, aerospace, biomedical and dental, to name the main ones.

Among all the advantages of AM, such as the above-mentioned complex design and customization, it is also valuable to mention the simplicity of the process that uses one machine and consequently a single production chain. This involves only one step for the process of component manufacture itself, except for the machine setup and the post-processing which depends on the part produced. On the other hand, the main drawbacks of AM processes can be identified in the limited volume available for manufacturing the part, since it is subjected to the chamber machine limit and the limited number of materials that can be processed with these technologies at this moment in time. In addition, post-processing is often required for AM parts due to layer by layer process and the superficial roughness of as-built parts can be high and not acceptable for components to be used in structural applications. Post-processing can be hardly automatized and it undoubtedly increases the already high overall cost of the process due to the high price of machines.

This work focuses on the production of an automotive component by means of Selective Laser Melting (SLM) process, an additive manufacturing technique that uses laser beam as the energy source acting on a metallic powder bed consisting of an aluminum alloy in this case.

SLM is a near-net shape process with limited post-processing machining required, depending on the final application. It produces few wastes thanks to the possibility of recycling the metal powder and enables optimized designs, rising opportunities for environmental advantages.

The use of aluminum alloys is still quite limited in critical structural applications (e.g., in case of fatigue loads) due to the formation of a large number of defects during the layer by layer process. However, Al alloys are favored in different applications in the automotive and aerospace field for their exceptional strength and stiffness-to-weight ratio.

The objective of this master thesis is to redesign an automotive component to be produced with the SLM process. The optimized design is obtained by using topology optimization algorithms and FEM analysis.

Every step in this work is aimed at demonstrating that with this technology is it possible to produce more complex geometries with reduced weight and high strength, subtracting material from the original outline parts, thanks to the design freedom. This thesis moreover shows that the performances of parts in the internal combustion engine (ICE) mechanism and, more in general, of the vehicle, can be improved with a reduced mass, and, consequently, a decrease in fuel consumption as well.

This thesis work is the result of the cooperation between Politecnico di Torino, McMaster University of Hamilton (Ontario, Canada) and STELLANTIS. The redesign, including the optimization, and printing of the part has been developed with the help of the research group of Prof. Elbestawi at McMaster Automotive Resource Centre (MARC), McMaster Innovation Park. The software used for CAD modelling is Solidworks® while the Finite Element (FE) analysis, the topology optimization and the design of support structures are performed in Altair Inspire®.

2. Part selection

The component chosen for the analysis carried out in the thesis is the piston of a four-stroke engine. Considering reciprocating engines, one of its main sub-systems is represented by the crank mechanism, which among the other parts is constituted by a certain number of pistons. A piston is one of the moving components contained by the engine cylinder, whose objective is to transfer the forces from the expanding gas in the combustion chamber to the crankshaft. For this project, a piston designed for a four-stroke engine and for a conventional production with slush casting is considered. In particular, the original part consists of a piston with an overall volume of 135.09 cm^3 and made of aluminum alloy 2017 A, with a total mass of the part of 379.161 g. The CAD model is shown in different views in Figure 1 and the drawing of the part with main quotations is shown in Figure 2.

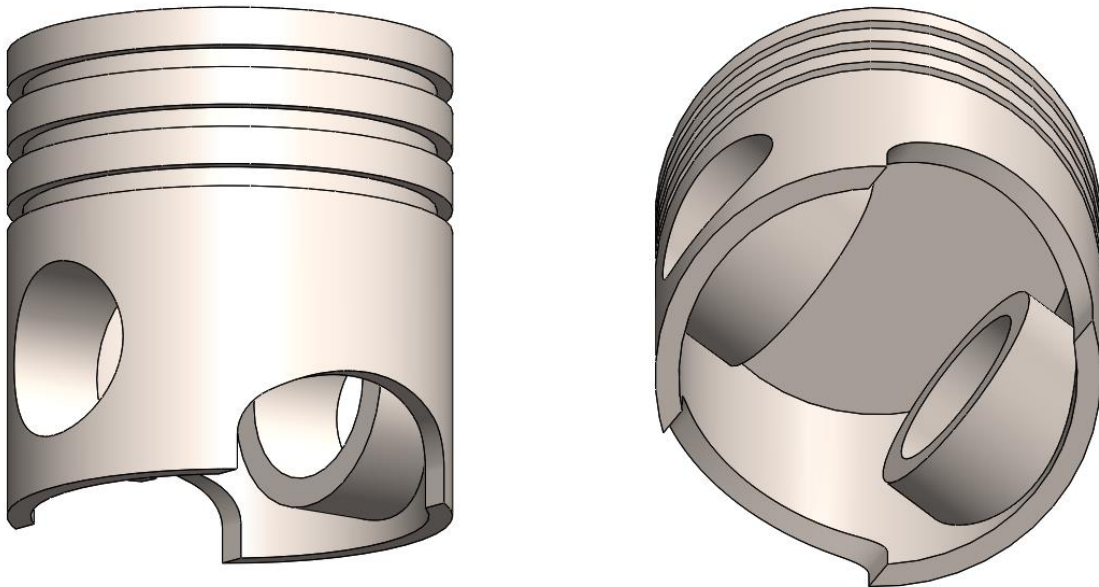


Figure 1 CAD model of the baseline piston (isometric and internal views).

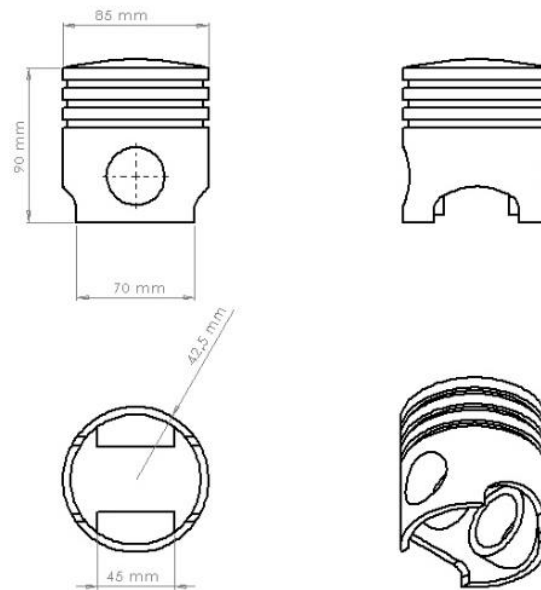


Figure 2 Piston drawing with main quotations in mm

2.1 Load cases

This section is dedicated to the dynamic analysis of the operating conditions of the piston in the internal combustion engine (ICE) considering the most significant load cases. For the analysis of this component, it is important to distinguish between two limit conditions reached by the crank mechanism, corresponding to the *top dead centre (TDC)* and the *bottom dead centre (BDC)* and to assess which is the most critical one.

The primary *Degree of Freedom (DoF)* of the piston is the translational one along the cylinder axis and, despite the limited gap between piston and liner, of about 0.05-0.1 mm, the piston has other two movements involving its secondary DoFs, i.e., the translation perpendicular to the cylinder axis and the rotation around the pin axis (*tilting*). These secondary movements are named "*piston slap movements*" and the forces related to them are:

- the gas force, F_g
- the thrust force F_n and the resultant force F , exerted by the connecting rod through the pin and directed along the cylinder axis
- the reaction force of the liner, F_l .

Schematic representation of the force's distribution is reported in Figure 3.

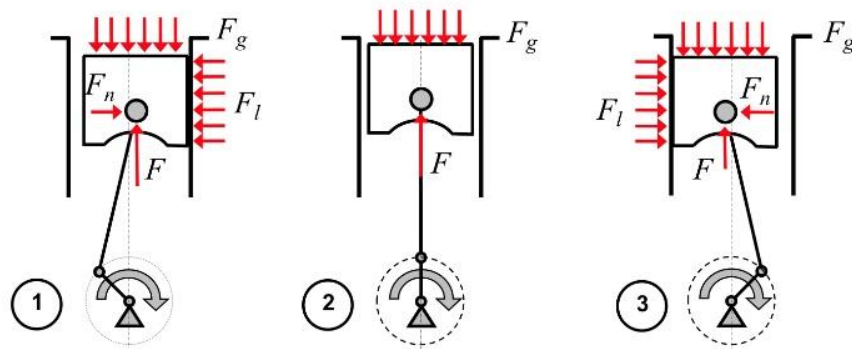


Figure 3 Forces exerted on the piston

As reported in Figure 4, during the overall engine cycle, the thrust force F_n changes its sign several times, causing the lateral movement of the piston inside the liner, being most critical during the initial expansion phase (0° , 720°), when F_n changes sign more quickly and reaches its maximum value.

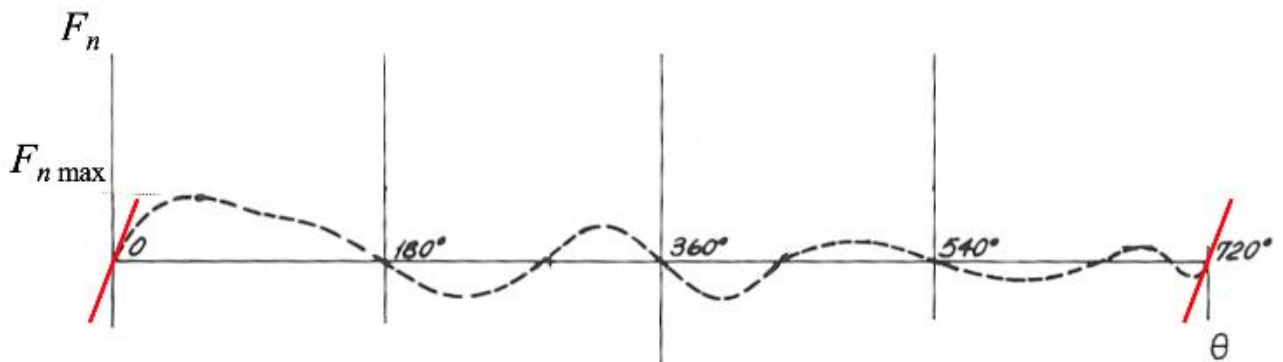


Figure 4 Trend of the thrust force during the engine cycle.

Referring to Figure 3, the vertical forces acting on the part can be oriented upward, due to inertia, or downward, if generated by the gas force right after combustion. According to the work done by I. Bhavi et al. [1], Figures 5 and 6 show the trend of the vertical forces acting on the piston top due to inertia and gas pressure respectively, while in Figure 7 the overall piston acceleration due to the combination of these effects for each crank angle after TDC firing (a_{TDCf}) of the engine cycle is reported.

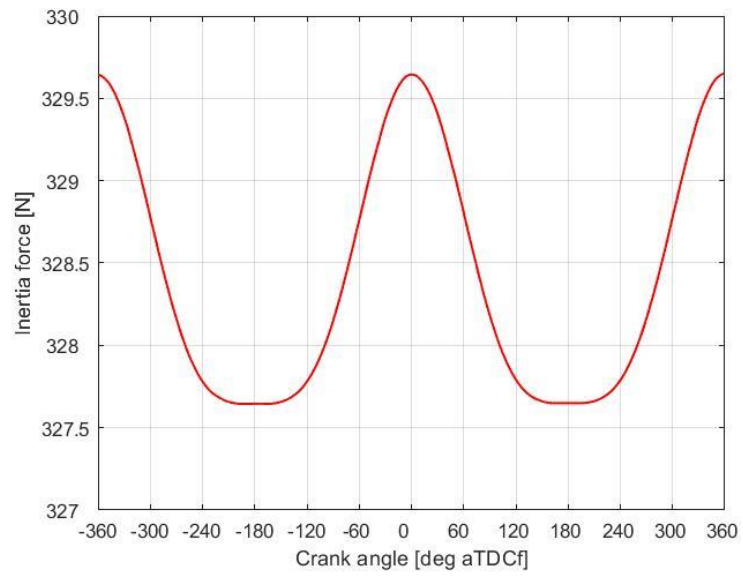


Figure 5 Variation of inertia force with crank angle [1]

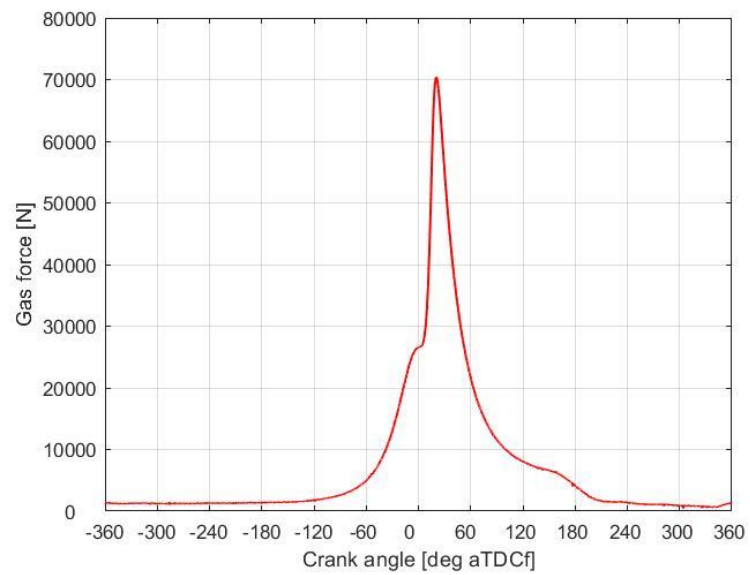


Figure 6 Variation of gas force with crank angle [1]

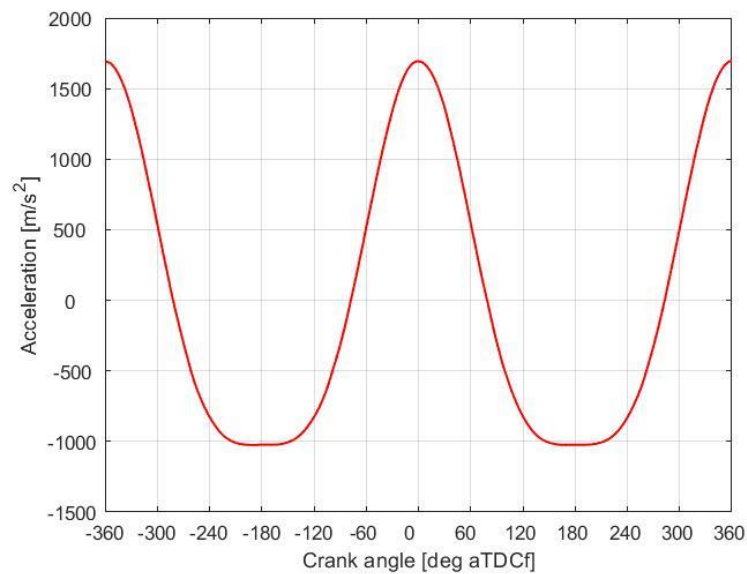


Figure 7 Variation of piston acceleration with crank angle [1]

According to Figures 5-7, the forces that arise when the crank mechanism is at the TDC are more severe than the ones that arise at the BDC, making the TDC the most critical condition for the piston and hence the case of interest for this work. The pressure applied on the piston top is evaluated considering the maximum gas force divided by the piston top surface itself. The result is a pressure of 12.418 Mpa and it is presented in Figure 8 with the red vector P.

2.2 Constraints

As seen in the previous paragraph, the piston is subjected to the direct action of gas and inertia forces. In order to develop a complete FEM analysis, it is essential to consider also the constraints to which the part is subjected. The piston is connected with the connecting rod by means of the wrist pin. This connecting element consists in a hollow cylinder with tapered ends, thicker in the middle to reduce the reciprocating masses, that is inserted into the piston hubs and passes through the small eye of the connecting rod. The latter is the component which links the piston and the crankshaft and transforms the piston's reciprocating motion in the rotating motion.

In this case study, this pin constraint is simulated by adding a support for each piston hole center not belonging to the part design space. In Altair Inspire® environment, supports are tools used to hold a part, in this case the piston cylindrical holes, so it doesn't move when loads are applied to it. In this way, the load condition related to the constraint is a rigid connection with all the degrees of freedom locked and a distributed support among all the cylindrical internal

surface of the hole. This configuration can be appreciated in Figure 8 where the red area represents the support distribution.

In this way it is possible to distribute in a more realistic way the load imposed by the connecting rod so to analyze the deformation of piston eye and the interaction between wrist pin and piston by considering the wrist pin as a rigid body and not focusing on its deformation.

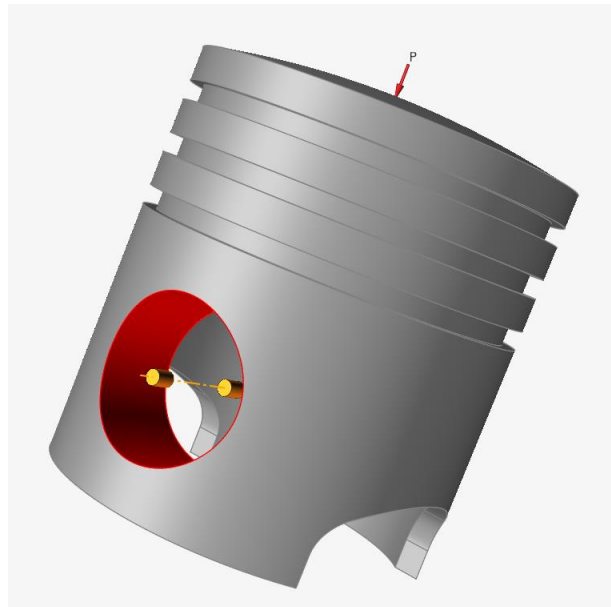


Figure 8 Piston constraints

2.3 FEM analysis on the original part

Once the load cases and the constraints have been defined, a Finite Element model of the piston can be created, by considering the original material, the aluminum alloy 2017A, also known as AlCu4MgSi and its chemical composition is reported in Table 1.

<i>Element</i>	<i>Nominal Chemical Compound</i>
<i>Fe</i>	0.7%
<i>Cr</i>	0.1%
<i>Mg</i>	0.4-1%
<i>Si</i>	0.2-0.8%
<i>Mn</i>	0.4-1%
<i>Cu</i>	3.5-4.5%
<i>Zn</i>	0.25%
<i>Al</i>	Res.

Table 1 AlCu4MgSi Chemical composition

2017A alloy is used, thanks to its high strength with simultaneously good workability, in the aerospace and automotive industry and it is one of the alloys of the 2xxx family: aluminum alloys in which copper is the main alloying element. It is characterized by high mechanical properties and fatigue resistance together with low corrosion resistance. In particular, the higher strength and hardness with respect to the other aluminum alloys, are due to the relevant presence of copper.

Table 2 shows the mechanical properties of this alloy, which are the input for the analyses carried out in this section.

E	G	ν	T_{sol}	T_{liq}	C_p	α	ρ	λ
MPa	MPa	-	°C	°C	J/(kg·K)	K ⁻¹	Kg/m ³	W/(m·K)
72500	27200	0.33	510	645	873	22.9·10 ⁻⁶	2790	134

Table 2 AlCu4MgSi - Mechanical properties

A static analysis of the investigated part in a steady state has been carried out with the commercial software Altair Inspire®. Steady state refers to an equilibrium state of the system which, accordingly, all the applied loads in the system are balanced by the constraints, and the system remains at rest ($v=0$). When solving a static analysis, all Finite Element (FE) solvers will solve the Equation:

$$Kx = f \quad (1)$$

Where:

- K is the global stiffness matrix
- x is the displacement vector response to be determined
- f is the vector of the external forces applied to the structure

An element size of 0.8 mm has been considered for the model. At first, the safety factor, reported in Figure 9, is analyzed. This factor of safety result type shows which areas of a model are in danger of yielding due to stress. The factor of safety for each part's material is considered when determining the overall factor of safety (SF) for the model. It is calculated according to (2).

$$SF = \frac{\text{material yield stress}}{\text{von Mises stress}} \quad (2)$$

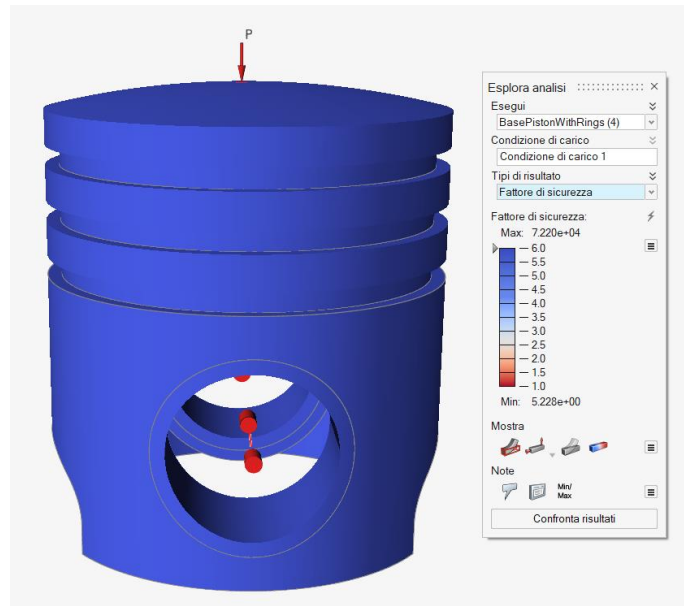


Figure 9 Factor of Safety - Baseline piston in AlCu4MgSi

As reported in the scale on the right in Figure 9, the areas with a safety factor approaching the minimum value of 1.0 are shown in red. In these regions, the part is most likely to fail. Since the minimum detected safety factor is 5.228, it is not in danger of failing for the considered load cases.

The next important result is the Von Mises stress distribution reported in Figure 10.

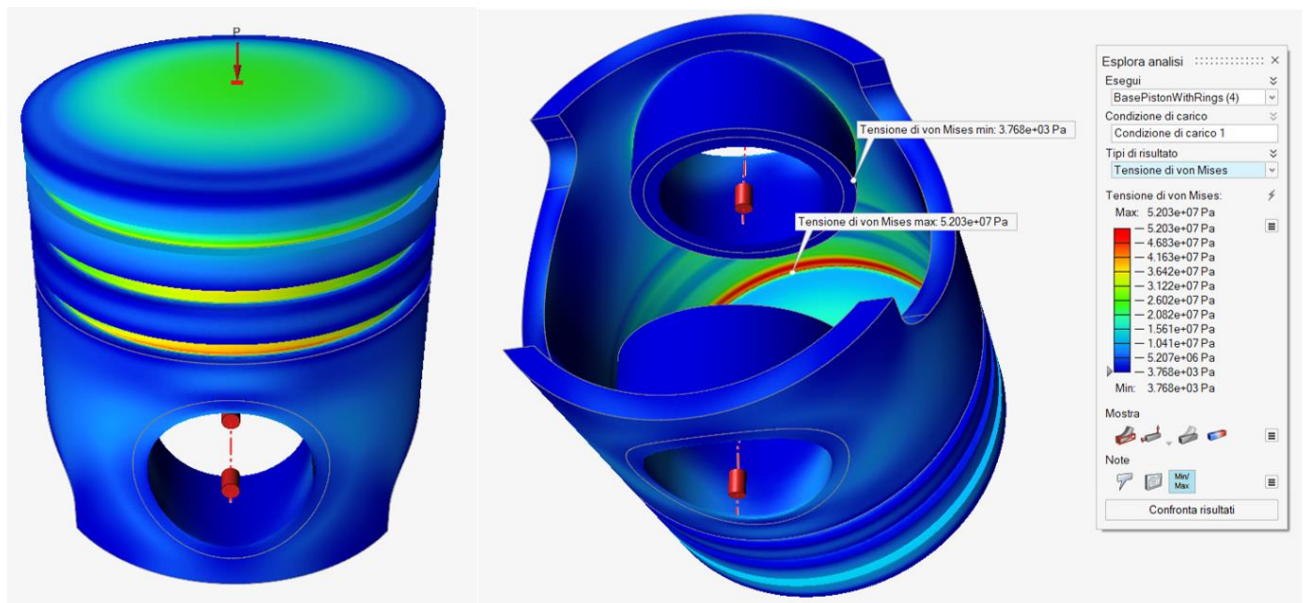


Figure 10 Von Mises Stress - Baseline piston in AlCu4MgSi

Von Mises stress ranges from a minimum value of $3.768 \cdot 10^{-3}$ MPa up to a maximum value of 52.03 MPa. Moreover, as it is clearly visible from the results reported in Figure 10, Von Mises stresses are distributed almost homogeneously over the whole component, even if it is possible

to identify some areas that are more stressed than the others. The most stressed one corresponds to the internal edge of the piston, at the connection of the top part of the component with the lateral surfaces. Also, the grooves for the rings' housing appear to be more stressed than average.

The last result analyzed is the distribution of tension and compression stresses on the part, shown in Figure 11. The distribution of areas subject to compression and those subject to tension are consistent with the physical condition of the piston at the point of TDC.

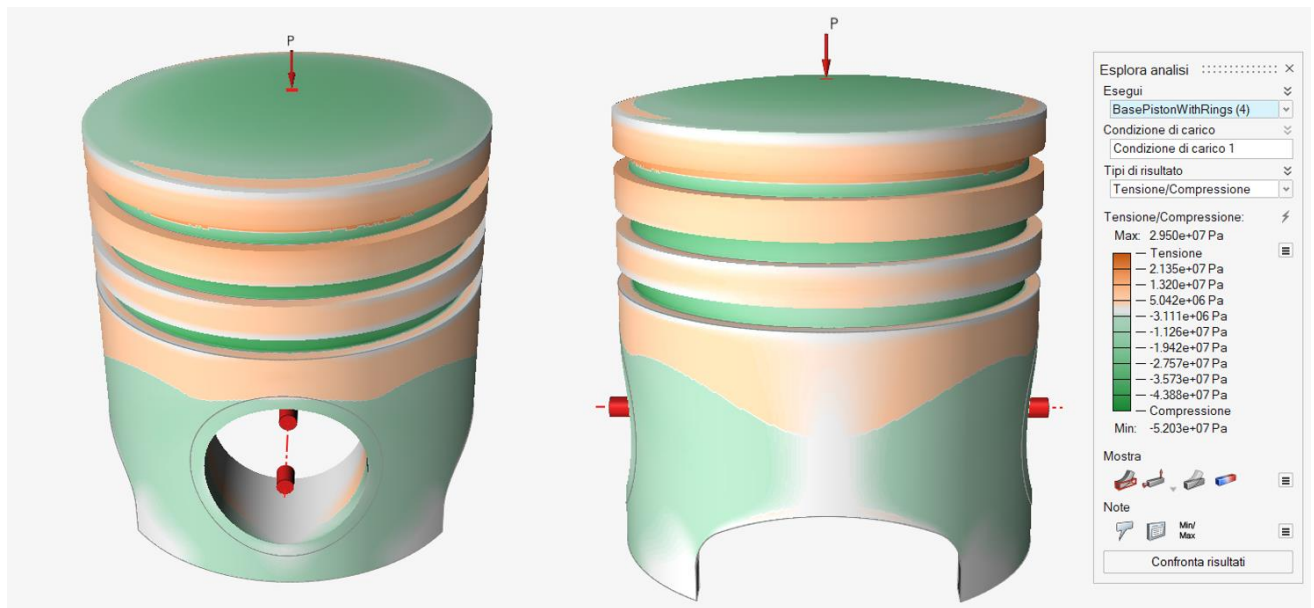


Figure 11 Tension/Compression Stress - Baseline piston in AlCu4MgSi

3. AM Process configuration

3.1 Selective Laser Melting

According to ISO/ASTM standards, AM technologies can be subdivided into seven categories, depending on the energy source and on the techniques used to create layers, and fuse the material. Each of these categories, briefly listed and described below, includes different types of processes.

- Vat photopolymerization – VPP: is a process in which the material is a liquid photopolymer in a vat and it is selectively cured by light-activated polymerization.
- Material Extrusion – MEX: in this case the material is in solid state and it is selectively dispensed through a nozzle. This family of processes is common for thermoplastic materials.
- Material Jetting – MJT: material in liquid form is selectively deposited in droplets form.
- Binder Jetting – BJT: in this process the material is in powder form and layers are joined with a liquid bonding element.
- Powder bed fusion – PBF: a thermal energy source fuses region of a powder bed.
- Directed energy deposition – DED: fusion process in which the material is melted as it is deposited on the previous layer.
- Sheet lamination: a part is formed by bonding sheets of material.

The Selective Laser Melting (SLM) process, used in this case study, belongs to the class of powder bed fusion technologies and for this reason is also referred to as Laser Powder Bed Fusion (L-PBF). The energy source is a high intensity laser that directly melts the material in powder form, layer-by-layer, according to the file format provided. The 3D CAD file of the part is converted into file '.STL' format, where STL is the abbreviation of "stereolithography". Upon the conversion from CAD format to .STL file, only the surface information of the part is kept while the constructive solid geometry (CSG) representation of how the geometry was created is lost. All the information needed to fabricate the part are in the .STL file and the solid model of the part itself is in the form of a surface geometry composed of triangular elements. Each of them is defined by three vertices and a normal vector composing a shell. As with the CAD file, the .STL representation of a part could be altered to modify the finished part's performance [2]. Starting from the CAD file of the component to be printed, the steps to be followed to manufacture a component with the SLM process can be divided are the following:

1. CAD file is converted in .STL file;

2. STL file is processed by specific software, Altair Inspire® in this case, to provide the appropriate support structures where needed. Supports are necessary to avoid failure during the printing phase of the part if it has a complex shape. The software of the printing machine also generates a number of slice data for laser scanning of every layer;
3. Inside the building chamber, the first thin layer of metal powder is spread on the building plate to prepare for the printing phase and, to minimize oxidation and to protect the heated metal parts against oxidation, the oxygen content is decreased below 0.1% by argon gas injection in the chamber itself.
4. Printing phase: the high energy density laser melts and fuses specific zones of the powder bed thin layer according to the input .STL file. The building plate is moved downward, and a new layer of powder is spread on top of it by the recoater blade. Now the laser is ready to scan the subsequent layer until the component is completed.
5. Loose powder removal and recycling.
6. Removal of parts and supports from the building plate.

In Figure 12 this procedure is shown.

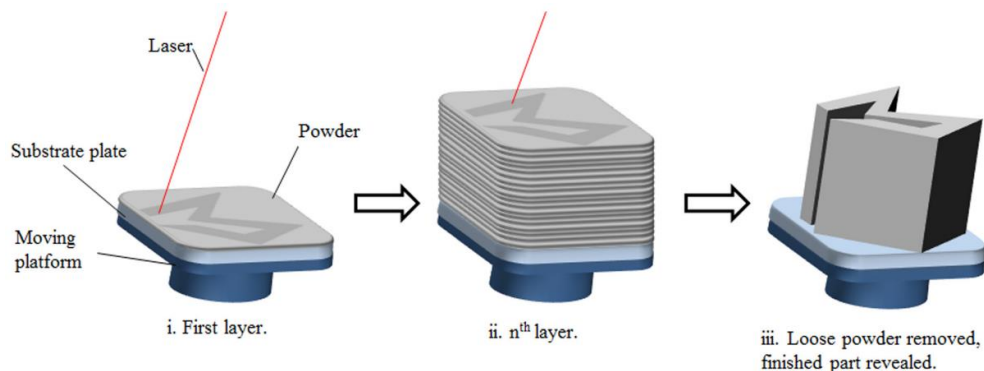


Figure 12 SLM process. (i) High-power laser melts selective areas of the powder bed. (ii) Process is repeated for successive layers. (iii) Loose powder [3]

The process parameters of the printing phase must be adjusted such that a single laser vector can fuse completely with the nearby melting vectors and the preceding layer. These parameters play a fundamental role in the evaluation of the volumetric energy density used to heat up and melt the powders. Process parameters used for this work study will be analyzed later in detail. Other than the above-mentioned advantages of the AM, literature works shown that the SLM process produces fully dense near net-shape components without the need, depending on the application and on the type of applied load, for post-processing, other than the removal of parts and supports from building plate, step 6.

Another favourable aspect of SLM is the possibility to recycle the powder that is not used during the process. Despite this, since the powder has been subjected to a thermal history that may have altered its mechanical properties, the recycled powder should be used in reasonable proportions together with fresh powder for new printings.

The materials that can be processed with SLM process are several, with stainless steel, nickel-based super alloys or cobalt-based super alloys and light alloys being the most widespread. Light alloys include titanium alloys, such as Ti6Al4V, aluminium alloys, like AlSi10Mg, and Maraging steel. The choice of the material used in this work is analyzed and justified in the following paragraph.

3.2 Material selection and powder characterization

As mentioned in section 2.3, the aluminum alloy used for the original part is widely used in the automotive and aerospace industries. For these purposes, AlCu4MgSi is processed by casting associated with solution annealing and subsequent natural ageing to develop its potential and to obtain the best mechanical performances. For Additive Manufacturing processes, however, AlCu4MgSi cannot be processed because the presence of copper generally increases the crack sensitivity of the alloy and, during the printing process, cracks can easily form along the grain boundaries. In particular, as can be seen from Figure 13 and considering Table 1, the copper content below 4.9% corresponds to a very high level of relative crack sensitivity for the AlCu4MgSi alloy.

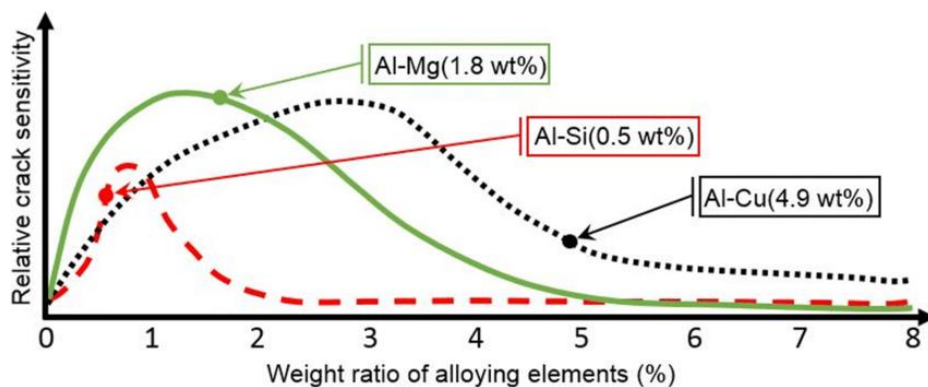


Figure 13 The effect of alloying elements on the relative crack sensitivity of aluminum alloys [4]

For this reason, the material chosen for this case study is not AlCu4MgSi but AlSi10Mg, another interesting material among aluminum alloys that is also one of the most used in the AM field. The combination of achieving dynamic load capacity while maintaining high strengths enables it to be used for highly stressed parts and therefore components made of this material are ideal

to be used in aerospace engineering and the automotive field as well. This AlSi alloy has a high concentration of silicon (more than 9%), which reduces the thermal expansion of the part. The hypoeutectic alloy is near the eutectic composition (12.5% Si) which is responsible for the excellent casting properties together with a small solidification temperature range. In Figure 14 the phase diagram of Al–Si is shown [5].

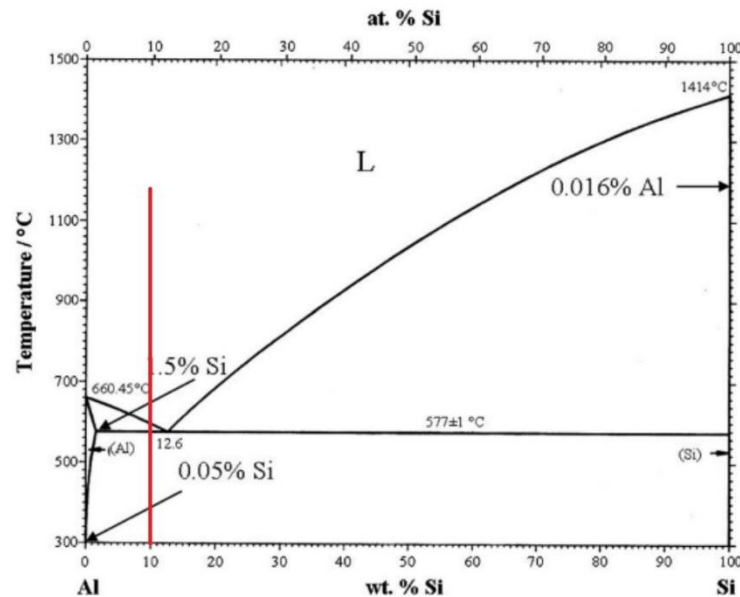


Figure 14 Al-Si phase diagram [5]

The red line in the phase diagram corresponds to the alloy composition for this case study. Table 3 reports the chemical composition of the AlSi10Mg alloy used.

<i>Element</i>	<i>Nominal Chemical Compound</i>
<i>Fe</i>	0.13%
<i>Ti</i>	0.01%
<i>Mg</i>	0.01%
<i>Si</i>	9.80%
<i>Mn</i>	0.35%
<i>Cu</i>	0.05%
<i>Al</i>	Res.

Table 3 AlSi10Mg Chemical composition

The presence of magnesium, up to 10%, strengthens and increases the hardness of alloys by solid solution without a considerable decrease of ductility, while the silicon improves the castability of aluminium alloys due to a better fluidity and a lower solidification shrinkage. The latter also increases the strength and the abrasive wear resistance. In a combination with Mg,

silicon allows strengthening this alloy through the precipitation of Mg_2Si (precipitation hardening).

For the above-mentioned reasons and for its characteristics, AlSi10Mg spherical gas atomized powder with particle size in the range of 27-40 μm has been chosen for the production of the component with the SLM process. Since the SLM process relies on thin layers of powder spread and melted selectively by the laser, the powder feedstock quality is of paramount importance, and it can be evaluated in terms of extrinsic and intrinsic properties. In Table 4 the most relevant powder features for this case study are reported and for each property, the American Society for Testing and Materials (ASTM) standard is specified.

	<i>ASTM standard</i>	<i>Value</i>	<i>Units</i>
<i>Hall flow rate</i>	B213	74	s/50g
<i>Apparent density</i>	B212	1.34	g/cm ³
<i>PSD – sieve analysis</i>	B214	+63	μm

Table 4 AlSi10Mg powder characterization

The characteristics of the AlSi10Mg powder reported in Table 4 are extrinsic properties since they are strictly related to powder morphology, not to its chemical composition, and they can affect the quality of the additively manufactured part.

Hall flow rate is a measurement of the powder flowability determined by Hall funnel according to the ASTM B213 standard [6]. Its value represents the time in seconds of a weighted mass (50.0 g) of metal powder to flow through the calibrated orifice of a Hall Flowmeter funnel. This measurement is relevant in this case study because flow properties influence production rates and uniformity of the powder bed and thus the final result of the printed parts. The ability of a powder to flow is inversely proportional to interparticle friction and it can also be affected by humidity and moisture content [6].

Apparent density is also assessed using the Hall funnels according to the ASTM standards B212 [7] and it is a measurement of the actual volume occupied by a mass of loose powder. As for the Hall flow rate, apparent density also affects the uniformity of the powder bed and layer distribution by the recoater during the printing process. Material density, particle size, particle size distribution (PSD), particle shape, surface area and roughness of individual particles, and particle arrangement are all factors that influence the apparent density. It is directly proportional to particle size; this can be explained considering that smaller particles have

greater specific surface, and this factor increases the friction between particles and subsequently decreases the apparent density. On the contrary, it is indirectly proportional to particles' surface roughness, and it also decreases when particle shape becomes less spherical and more irregular. Gas-atomized particles, as the powder analyzed in this section, exhibit very low friction thanks to their spherical shape.

Particle size distribution (PSD) is evaluated by means of sieve analysis according to ASTM B214 standard [8]. During this testing procedure, powder passes into a series of sieves, each of them with progressively smaller mesh sizes, while the stack of sieves is vibrated. The mass of powder that is collected by each sieve as a fraction of the total mass is recorded with the respective sieve size.

3.3 Process parameters optimization

The main objective of this section is to find the optimal process parameter-set, to enhance mechanical properties like density, defects and microhardness. The influence of Selective Laser Melting process parameters, such as laser power, scan speed and hatch spacing, on the mechanical properties of AlSi10Mg alloy builds is investigated, using a design of experimental (DoE) approach correlated with the energy density model discussed in more detail below in this chapter. Optimum process parameters are obtained by driving this experimental method to maximize the part's density. Once the parameters have been identified, tensile properties are experimentally assessed in order to design the AlSi10Mg component to be produced with the Selective Laser Melting process.

The SLM machine used in this study is an EOS M290 having a 400 W Yb fiber laser with a focus diameter of 100 μm in a building chamber under the protection of a high-purity argon gas atmosphere with oxygen content below 0.1% to minimize oxidation.

3.3.1 Process parameters overview

Starting from the composition of the metal powder reported in Table 3, process parameters must be identified to maximize the density and minimize the porosity to achieve a high quality of the final parts. The comparison between parts fabricated by the SLM process under different sets of process parameters is often made considering the laser energy density [7]. Among them all, the most widely used in the literature is volumetric energy density, defined by the relation (3).

$$E_V = \frac{P}{v \cdot t \cdot h} \quad [\text{J}/\text{mm}^3] \quad (3)$$

Where:

- P , Laser power: total energy emitted by the laser per unit time
- v , Scan speed: the speed at which the laser spot is moved across the powder bed
- t , Layer thickness: the depth of each new powder layer to be melted
- h , Hatch spacing: spacing between neighbouring scan vectors, should be designed to allow a certain remelting of the previous weld track to guarantee full coverage of the region to be melted.

These quantities are schematically indicated in Figure 15.

By increasing scan speed and hatch spacing it is possible to improve the production rate, while a reduction of these two parameters causes an increase of volumetric energy density.

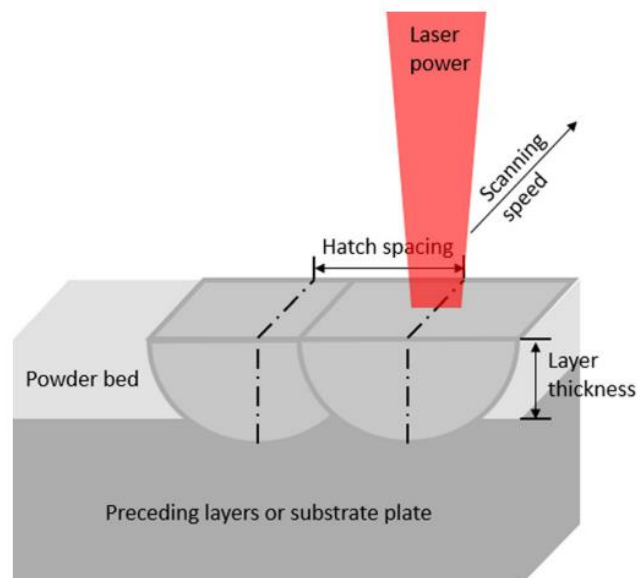


Figure 15 SLM process parameters: laser power, scanning speed, hatch spacing and layer thickness [3]

If the volumetric energy is insufficient, the melt pool will be small so the laser energy may not penetrate deeply enough to fully melt the actual powder layer and the top surface of the solid

layer below. This lack of volumetric energy can leave an amount of not melted powder between layers, resulting in porosity and risk of delamination. The schematic illustration of insufficient penetration is reported in the central scheme of Figure 16 in comparison with the efficient processing, on the left, and the keyhole phenomenon on the right.

Keyhole formation occurs whether the energy density is in excess, this can be due to several reasons as can be a high laser power or low scanning speed that leads to an excessive penetration of the laser into the metal under the layer of powder. This deep cavity of the melt pool can trap gas in a pore below the component surface affecting the microstructure of the solidified material [8]. As can be seen for Figure 16, keyhole defects are characterized by an almost spherical shape given by their formation mechanism since the gas bubbles are caught by the solidification front.

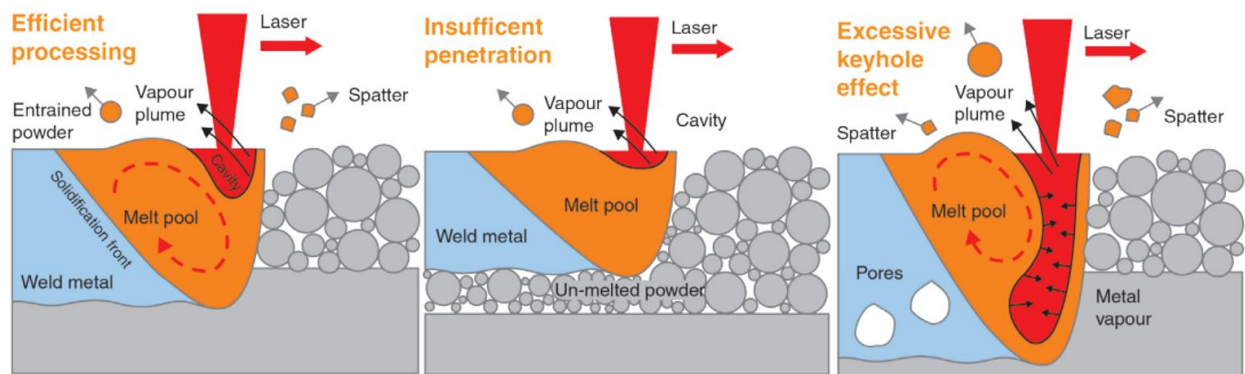


Figure 16 Schematic representation of efficient process, insufficient penetration and keyhole effect [8]

In addition, too large hatch spacing results in regular porosity in built parts because adjacent melt lines do not completely fuse together. Hence, a suitable combination of laser power, scanning speed, hatch spacing, and layer thickness is essential for SLM processing to successfully build near full-density parts [7].

According to the study conducted by Kempen et al. [9], it is possible to define a process window for AlSi10Mg based on the requirement of a continuous scan track for what concerns laser power and scan speed. This operating window is reported as the hatched red area in the processing map presented in Figure 17.

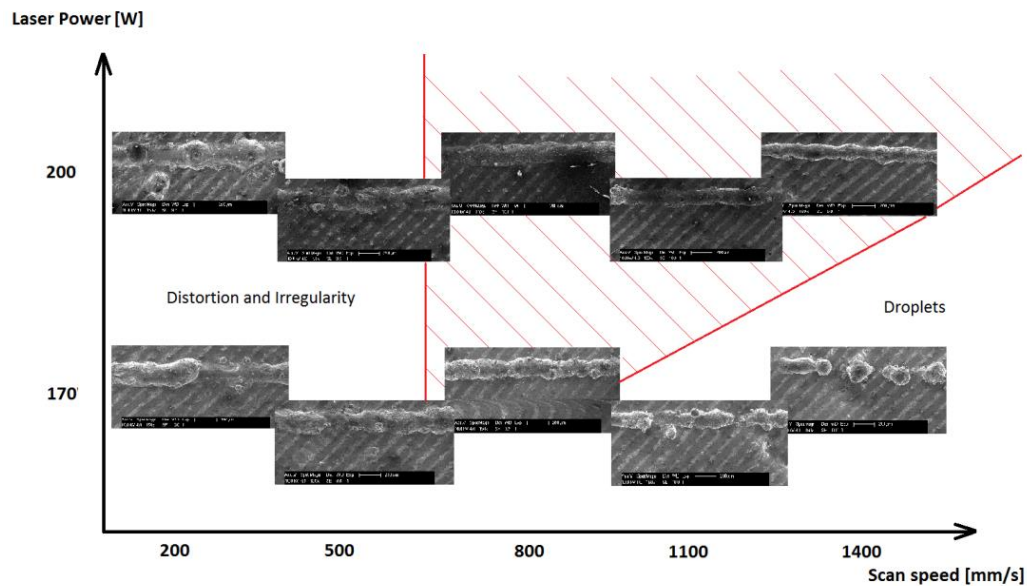


Figure 17 Processing map for SLM of AlSi10Mg, based on the top view of single-track scan [9]

It can be observed that low laser power (170 W) in combination with high scan speed (1400 mm/s) causes the formation of droplets and very poor wetting, thus a bad connection to the substrate. On the other hand, higher laser power (200 W) in combination with low scan speed (200 mm/s) causes a deep penetration and partial evaporation of the powder, resulting in distortions and irregularities as well as the keyhole effect seen previously [9].

To solve this multi-variable problem, the density of a set of samples containing 12 cubes with dimensions of 10x10x10 mm printed in AlSi10Mg with different laser powers, scanning speeds and hatch spacings has been experimentally assessed. The DoE is shown in Table 5.

Label	Power [W]	Speed [mm/s]	Hatch [mm]	E_v [J/mm³]
B	335	1050	0.15	70.90
D	335	1050	0.19	55.97
F	335	1300	0.15	57.27
H	335	1300	0.19	45.21
J	370	1050	0.15	78.31
L	370	1050	0.19	61.82
N	370	1300	0.15	63.25
P	370	1300	0.19	49.93
Q	352	1050	0.15	74.50
R	352	1050	0.19	58.81
S	352	1300	0.15	60.17
T	352	1300	0.19	47.50

Table 5 SLM process parameters applied for fabricating AlSi10Mg samples

This Design of Experiment considers 12 possible combinations of the following process parameters:

- Three laser powers: 335 W, 352 W and 370 W
- Two scan speeds: 1050 mm/s and 1300 mm/s
- Two hatch spacings: 0.15 mm and 0.19 mm

Layer thickness has not been investigated since considering the powder particle size of 27-40 μm and in agreement with the research done by Maamoun et al. [10] and by M. A. Balbaa et al. [7], a 0.03 mm layer appears to be the optimal solution for all samples.

For each set of the investigated parameters, the volumetric energy density has been evaluated. According to the results obtained by Maamoun et al [10], for AlSi10Mg there is an optimum range of the process parameters that allows to reach the highest possible relative density value of the part. This range, in terms of volumetric energy density, is between 50 and 60 J/mm^3 and it enables the production of high-density parts, reaching a relative density up to 99.7%. Beyond this range, the relative density is lower because of the lack of fusion at the lower energy density while balling formation (incomplete fusion due to poor penetration of the melt pool in the previous layer, the scan breaks into separated balls) or hydrogen gases trapped merge at higher laser power [10].

As illustrated in Figure 18, the scanning of layers is conducted using a scanning strategy that alters 67° between subsequent layers. This is done to provide a more homogeneous distribution of residual stress, as suggested from literature [10].

Results obtained for each sample in terms of density, defects and microhardness are presented in the next session.

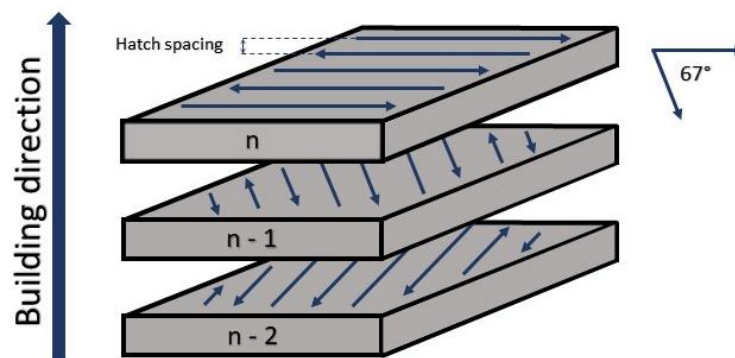


Figure 18 Scanning strategy

3.3.2 Experimental analysis

The objective of this section is to compare the results of the experimental analyses carried out on coupons, concerning densification level, defects in terms of porosity and keyholes, microstructure and micro hardness.

At first, the density of each coupon is assessed. Thereafter, the specimens are prepared for microstructural investigation with the optical microscope. As a first step, all samples are sectioned with a precision cutter along the building direction. The cross-cutting operation is performed using a 0.25-mm-thick diamond blade with a blade rotational speed of 3000 rpm. The samples are then mounted in Bakelite specimens, a thermosetting phenol formaldehyde resin, to proceed to the subsequent grinding and polishing stages. During the grinding stage, samples are subjected to the action of four different sandpaper with increasing grit while in the polishing stage, three different pads are used as the last step to obtain a mirrored surface.

After the polishing process, a chemical attack is conducted to highlight the microstructure of the metal by selective corrosion. In the present thesis work, Keller's reagent is used to highlight melt pools and scan traces of the as-built sample in the direction parallel to the Z direction. In Figure 19, cubes before and after sample preparation are shown.

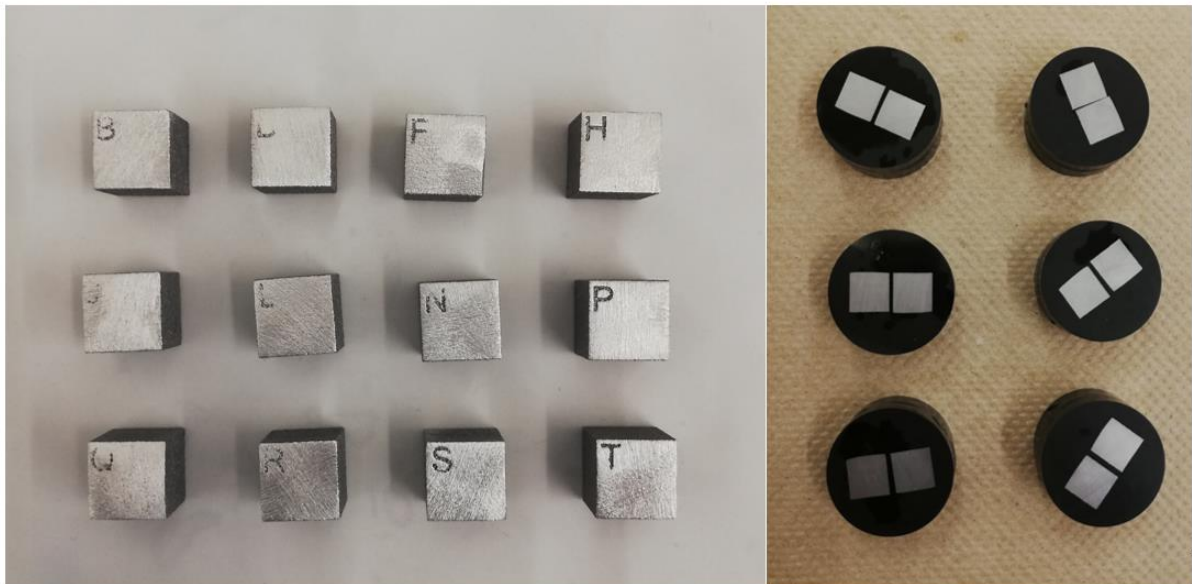


Figure 19 AISi10Mg cubes before and after sample preparation

Samples are subsequently analyzed using a Nikon LV100 optical microscope. This study focuses on the investigation of process parameters of the core of the samples, since the contour of the printed parts are usually modified by surface post processing such as shot peening or polishing to improve the quality of the final part.

3.3.2.1 Experimental results: densification level

The densification level of SLM cubes is measured using the Archimedes method according to the ASTM B962 – 17 standards [11]. Figure 20 shows the experimental setup adopted for the specimens in water and air.

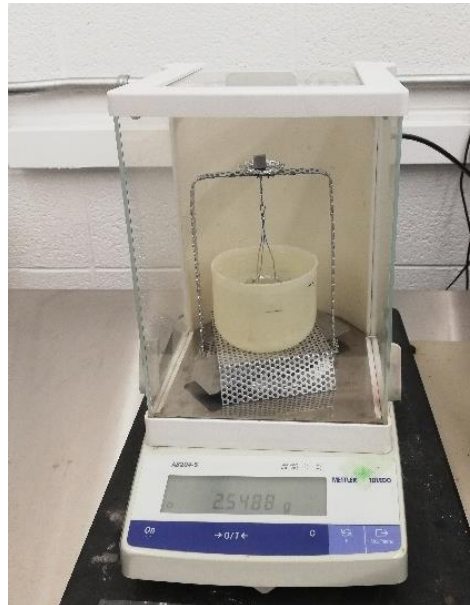


Figure 20 Weighing support for specimens in water and in air

Density measurements results of the samples are reported in Table 6, together with the volumetric energy density as a reference. To calculate the density, each cube is weighed in dry and wet conditions with a precision balance at room temperature, and the resulting density is computed according to relation (4).

$$\rho = \frac{\rho_d}{\rho_d - \rho_w} \quad (4)$$

Where:

- ρ density of the sample
- ρ_d dry density of the sample, evaluated as the ratio between the measured dry mass in air and the volume of the sample, which in this case is 1 cm^3
- ρ_w wet density of the sample, evaluated as the ratio between the measured wet mass in water and the volume of the sample.

This procedure is repeated twice for each sample and the resulting average between the two values is shown in the third column of Table 6, while the complete set of data is presented in Appendix section. Density results are also expressed as relative density [%] by taking AlSi10Mg's bulk density as 2.68 g/cm^3 .

Label	E_v [J/mm³]	Average density [g/cm³]	Relative density [%]
B	70.90	2.67	99.73
D	55.97	2.65	99.07
F	57.27	2.67	99.68
H	45.21	2.68	99.86
J	78.31	2.65	98.87
L	61.82	2.65	99.06
N	63.25	2.66	99.39
P	49.93	2.66	99.29
Q	74.50	2.65	98.79
R	58.81	2.66	99.20
S	60.17	2.67	99.52
T	47.50	2.67	99.63

Table 6 Samples density measurements

The highest value of relative density is 99.86% and it is obtained for sample H printed with a laser power of 335 W, a scan speed of 1300 mm/s and a hatch spacing of 0.19 mm. However, all measured relative densities are above the value of 98.79%.

The variation of relative density with respect to process parameters, i.e., scan speed, laser power and hatch spacing, is analyzed in Figures 21 to 24. In Figure 21, relative density is shown as a function of the scan speed, considering all the combinations of power and hatch spacing analyzed.

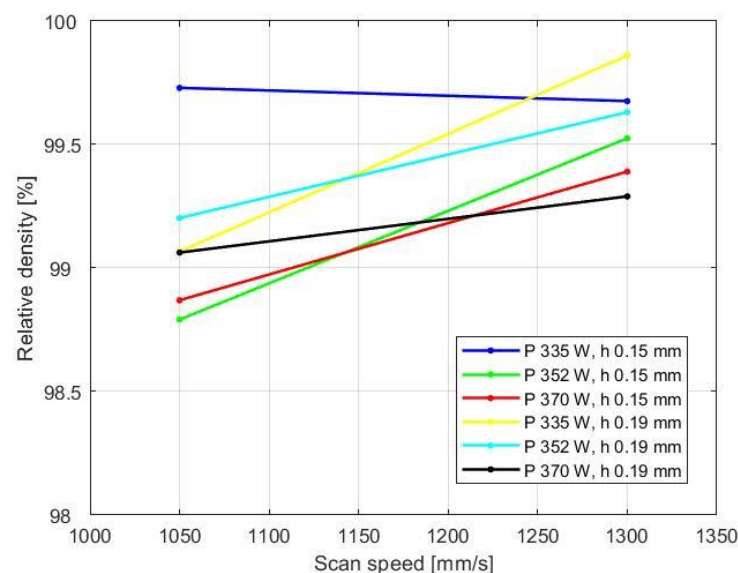


Figure 21 Relative density of AISi10Mg parts as a function of the scan speed

In agreement with [9], the relative density increases with the scan speed, and this is because the scan track becomes more stable leading to a diminution of defects.

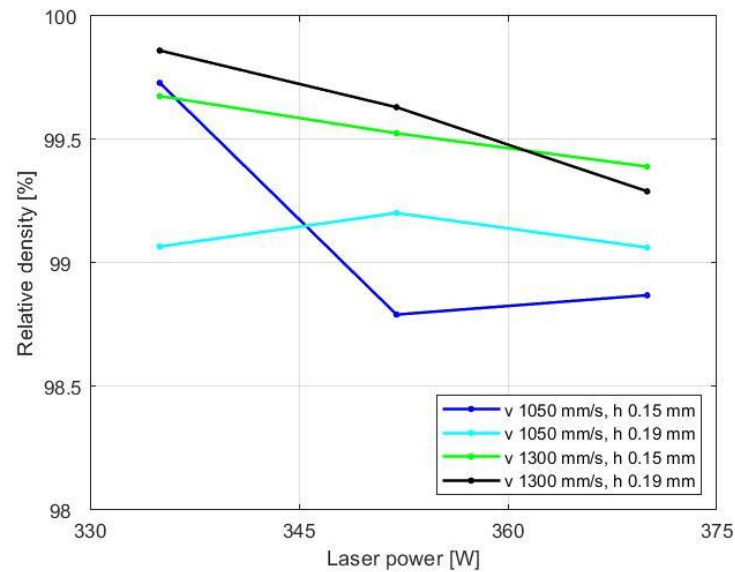


Figure 22 Relative density vs laser power

Here the trend is less evident compared to Figure 21. In general, it can be noted that the relative density of the specimens decreases as the laser power increases for the range of powers analyzed. This non univocal tendency can be explained through the interaction of process parameters, which are closely interrelated. For example, for a scan speed of 1050 mm/s and hatch spacing of 0.15, the trend is not clear, suggesting that this combination for input power above 345 W should be avoided.

In Figure 23, the relative density is presented as a function of the hatch spacing.

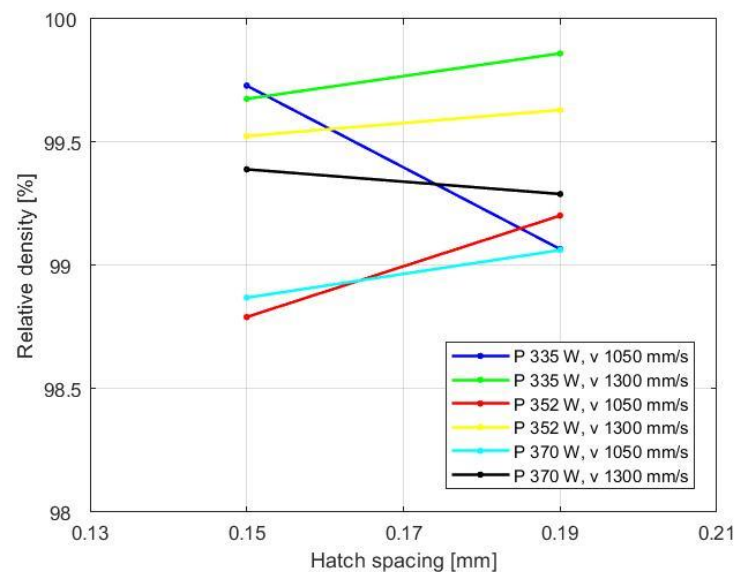


Figure 23 Relative density depending on hatch spacing

The general trend of this plot is opposite to the trend found by Buchbinder et al [12], according to which the relative density decreases with the hatch spacing. This can be explained

considering that the hatch spacing variation in this case study is extremely narrow since it varies from 0.15 to 0.19 mm thus its direct influence on density is not appreciable and, as a matter of facts, unified trend is not appreciable. Moreover, the trend found for an input power of 335 W and a scan speed of 1050 mm/s can be explained by the considering the experimental variability and that, for this configuration, a hatch distance of 0.19 mm induces a reduction of the relative density due to a strong interaction between process parameters.

To sum it all up, the relative density is plotted in Figure 24 as a function of the volumetric energy, previously defined in Equation (3). The volumetric energy is among the most significant parameters influencing the densification of the part since it condenses all the main process parameters, therefore providing a wider view of the topic. The experimental data in Figure 24 are fitted by a first order regression curve.

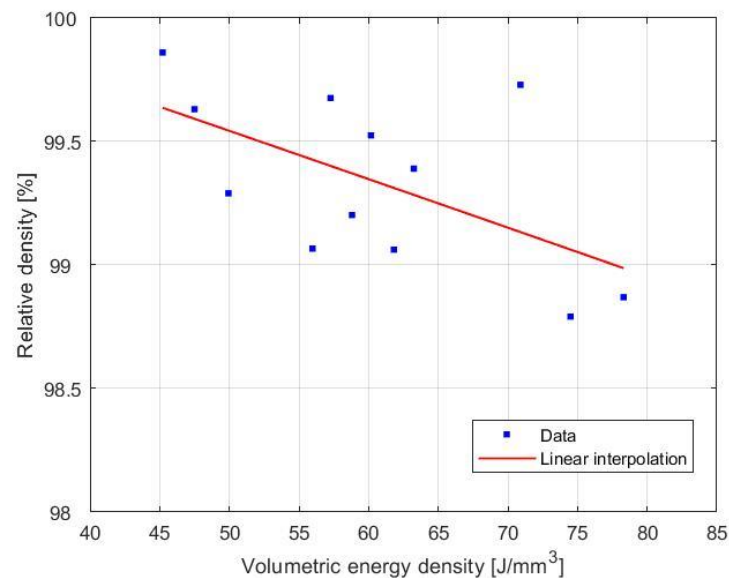


Figure 24 Relative density vs volumetric energy density

According to the work done by E. O. Olakanmi et al in 'A review on selective laser sintering/melting (SLS/SLM) of aluminum alloy powders: Processing, microstructure, and properties' [13], relative density, as a function of volumetric energy, reaches a maximum for a specific volumetric energy input and then decreases. In Figure 24, this trend is fulfilled, the higher density is reached for a value of 45.21 J/mm³ with, moreover, a large scatter. This result is in agreement also with the work done by Ahmed H. Maamoun et al. [10], by which the relative density of the part on the volumetric energy has a parabolic trend with a maximum in the range between 50 and 60 J/mm³. Particularly, as mentioned in section 3.3.1, at a low melted volume fraction obtained by using high scan speed, high hatch spacing and low values of laser power,

the liquid phase in the melt pool is not enough or has not sufficient time to enhance wettability. Meanwhile, at low scan speed, small scan spacing, and relatively high laser power, in this case study around 45 J/mm^3 , the amount of liquid phase generated is higher and solidification time is appropriate, thereby reaching the maximum density obtainable. This region corresponds to the peak value according to [10]. After reaching this peak, when volumetric energy is further increased, relative density decreases, this reverse trend between the two considered variables can be explained by the keyholes formation mechanism. The laser overpenetration caused by excess energy can trap gas under the surface of the part negatively impacting its density. The latter decreasing part of the curve is in indeed the one shown in Figure 24.

3.3.2.2 Experimental results: microhardness

Microhardness is measured considering 5 repeated indentations for each cube with a load of 200 gf for a dual time of 10 seconds according to the ASTM E92 – 17 standards [14] for Vickers Hardness. Results are reported in Table 7 together with the volumetric energy density and the standard deviation. The complete set of measurements is reported in the Appendix. To calculate the Vickers Hardness (HV), for each indentation, the mean Vickers indentation diagonal length is measured, and the resulting value is computed according to relation (5) following the ASTM E92 – 17 standards [14].

$$HV = 1000 \cdot 1.8544 \cdot \frac{F_{(gf)}}{d_{V(\mu m)}^2} \quad (5)$$

Where:

- $F_{(gf)}$ is the load expressed in grams-force
- $d_{V(\mu m)}$ is the indentation diagonal measured in micrometers

Values reported in Table 7 are the average of the 5 measurements for each cube.

<i>Label</i>	<i>E_v [J/mm³]</i>	<i>Average HV</i>	<i>Standard deviation</i>
B	70.90	122.8	2.31
D	55.97	126.8	2.86
F	57.27	127.6	1.62
H	45.21	130	5.58
J	78.31	121.6	1.47
L	61.82	122.8	3.87
N	63.25	126.8	3.71
P	49.93	125.4	3.01
Q	74.50	126.8	1.62
R	58.81	125.8	4.44
S	60.17	129.8	1.94
T	47.50	131.6	1.74

Table 7 Vickers Hardness measurements

From the values reported in Table 7, the hardness of the microstructure reaches a maximum of 131.6 HV for the T specimen, with a laser power of 352 W, a scan speed of 1300 mm/s and a hatch spacing of 0.19 mm. However, the average HV hardnesses are higher than the hardness of the chill cast alloys specified of AlSi10Mg by the European Standard EN 1706 for casting aluminum and aluminum alloys [15]. The rapid solidification experienced by the part during the SLM process affects the microstructures by creating a grain refinement which is one of the main reasons for the results achieved in this case study for what concerns the hardness.

In Figure 25, Vickers hardness as a function of the scan speed is shown, considering all the combinations of power and hatch spacing analyzed.

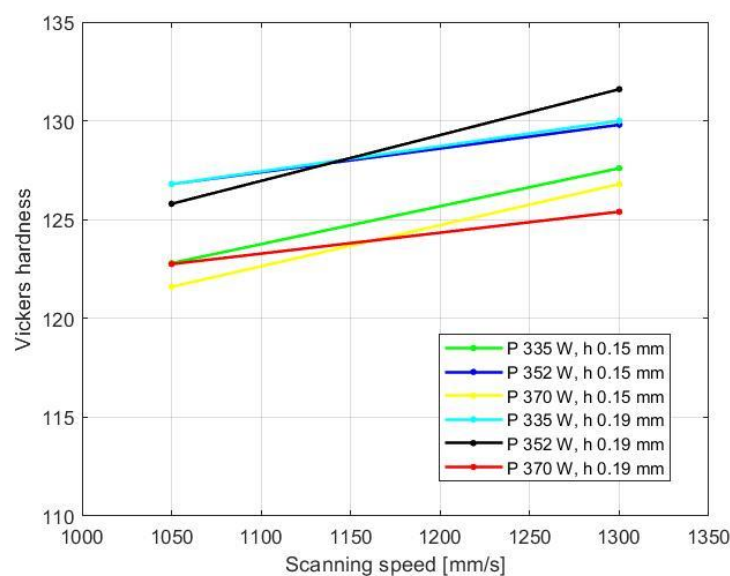


Figure 25 HV depending on scanning speed

The increasing trend in Figure 25 is in agreement with the one found by Ahmed H. Maamoun et al in 'The Effect of Selective Laser Melting Process Parameters on the Microstructure and Mechanical Properties of Al6061 and AlSi10Mg Alloys' [16]. The linear increase of the sample's hardness with the scanning speed can be explained with a lower solidification rate at low scan speeds. For a better understanding of this mechanism and in particular to correlate the laser scan speed and the solidification rate of the part, it is convenient to introduce the heat input as a measure of the energy deposited per unit length of the deposit and it is defined according to [17] presented in (6).

$$Q = \frac{P}{v} \quad (6)$$

Where P is the laser power and v is the scanning speed. For most of the alloys, higher heat input per unit length reduces the cooling rate making the microstructure coarser consequently leading to a decrease in hardness. As from figure 25, moving from 1050 mm/s to 1300 mm/s for the scan speed, hence decreasing the cooling rate, the Vickers hardness increases. This result is presented also by T. DebRoy et al in 'Additive manufacturing of metallic components – Process, structure and properties' [17] and it is consistent also with the following analysis of the hardness depending on laser power in Figure 26, for the lower range of laser power adopted.

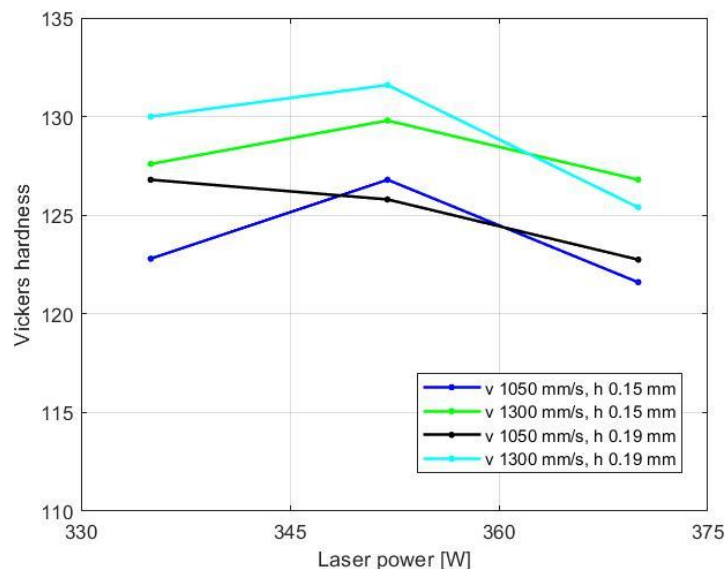


Figure 26 Vickers hardness depending on Laser Power

According to Figure 26, the hardness shows a peak for the intermediate laser power of 352 W. This result suggests that, for the investigated range, there is an optimal value of laser power ensuring the highest Vickers hardness.

Figure 27 plots the Vickers hardness in function of the hatch spacing.

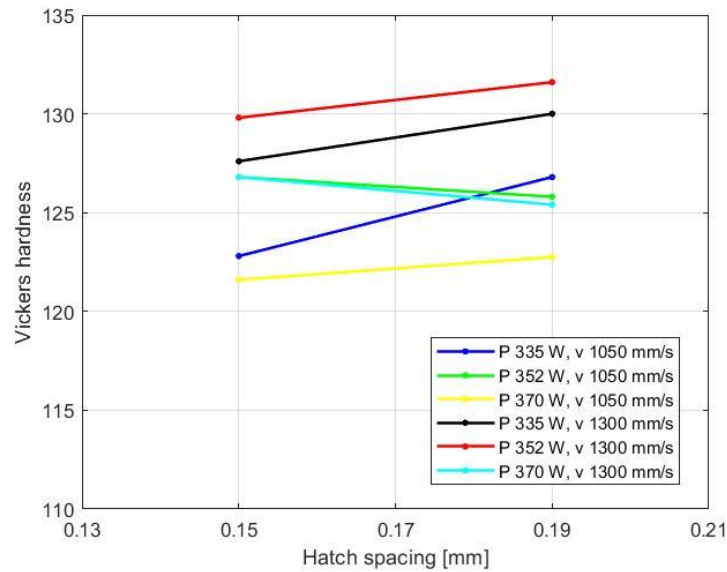


Figure 27 Vickers hardness depending on hatch spacing

According to Figure 27, the hardness is less sensitive to the hatch spacing if compared to the other investigated process parameters. This trend is confirmed by the work done by Buchbinder, D. et al in ‘High Power Selective Laser Melting (HP SLM) of Aluminum Parts’ [12] in which for parameters ranges, the hardness of the AlSi10Mg parts investigated is not affected directly by the hatch spacing.

Figure 28 plots the Vickers hardness as a function of the volumetric energy density.

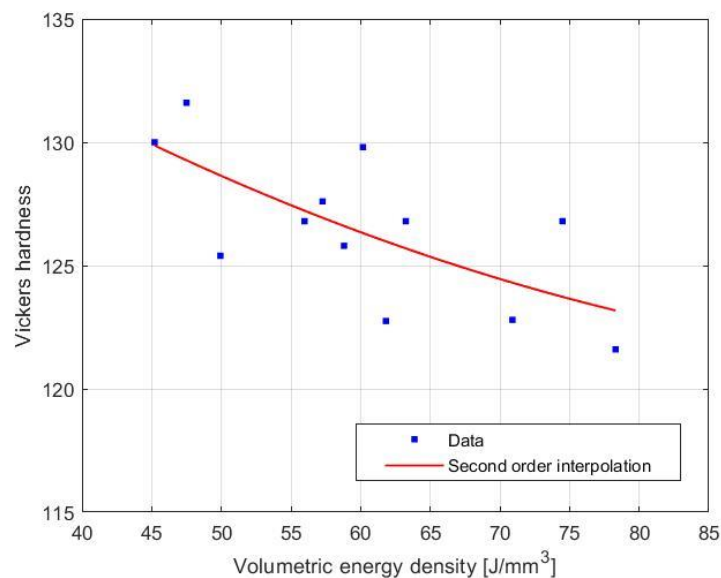


Figure 28 Vickers hardness depending on Volumetric energy density

The analyzed data are fitted by a second-order regression curve, showing that the Vickers hardness decreases when the volumetric energy increases. This experimental trend can be

explained once again by considering the keyholes formation mechanism. According to the work done by Ahmed H. Maamoun et al in ‘The Effect of Selective Laser Melting Process Parameters on the Microstructure and Mechanical Properties of Al6061 and AlSi10Mg Alloys’ [16], increasing the volumetric energy beyond the optimal value will promote keyhole occurrence and this negatively affects the hardness.

To conclude, the results of the experimental analyses carried out on the 12 cubes are summarized in Figure 29, which plots the relative density with respect to the Vickers hardness. Despite the large scatter, a relationship between the relative density and the Vickers hardness can be observed, with the hardness decreasing as the porosity of the part, inversely proportional to the density itself, increases.

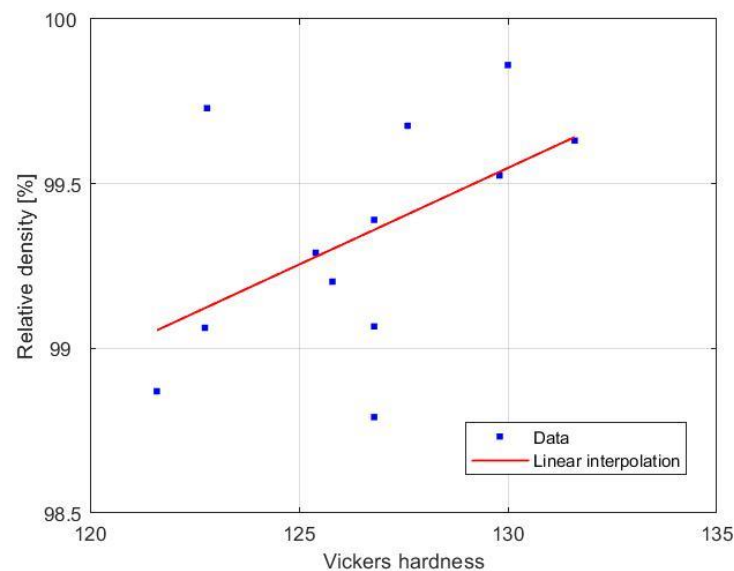


Figure 29 Relative density depending on Vickers hardness

3.3.2.3 Experimental results: microstructural defects and meltpools

This section focuses on the micrographs obtained with Nikon LV100 optical microscopy at a magnification level of x50 on as-built samples of AlSi10Mg, along the building direction (z direction). Accordingly, defects and porosities can be analyzed and correlated to the process parameters and their interaction, to the presence of impurities on the metal powder, to the low laser energy absorption, to problems of wettability of the solid fraction by the liquid phase, to the atmospheric conditions in the building chamber or to evaporation of some of the elements of the alloy. The analysis carried out in this section also aims at correlating the microstructure to the macroscopic properties of each sample.

For instance, Figure 30 illustrates process-induced porosity of irregular shapes formed inside the T sample characterized by a volumetric energy density of 47.50 J/mm^3 . For this sample, no keyholes are detected since the energy density value is inside the optimal operating window for AlSi10Mg.

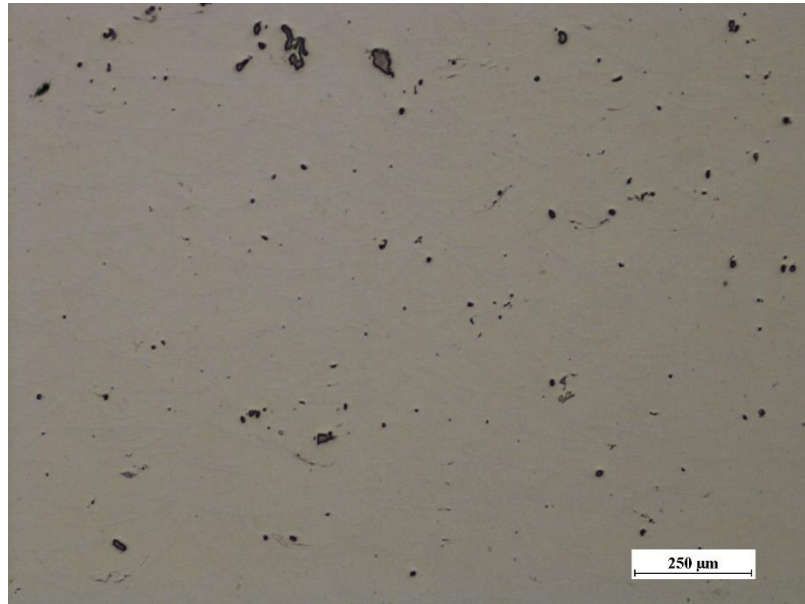


Figure 30 Microstructure of the as-built AlSi10Mg T sample

Increasing the energy density, keyholes appear in the microstructure. An example is reported in Figure 31 by the microstructure of sample J, which is characterized by an energy density of 78.31 J/mm^3 , the highest among all the analyzed cubes.

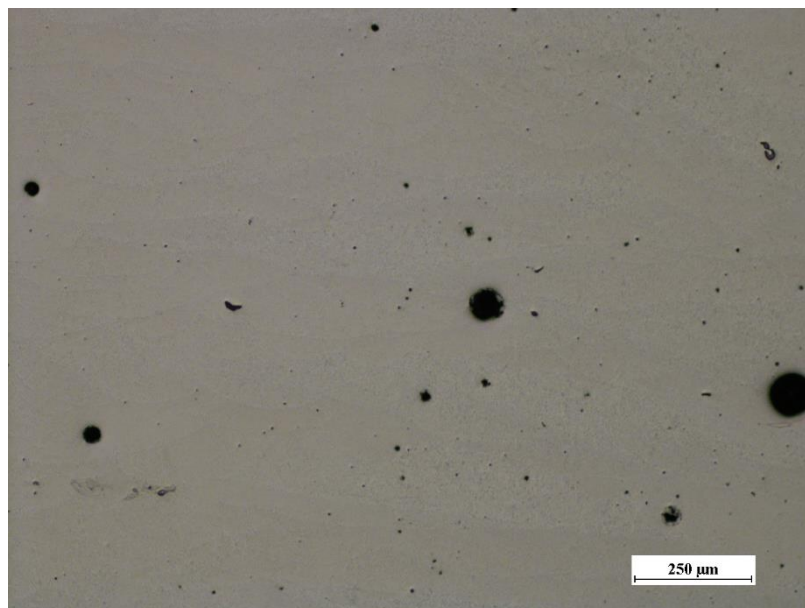


Figure 31 Microstructure of the as-built AlSi10Mg J sample

The plot shown in Figure 24 is here reported, together with the images of the microstructures of four selected specimens. This plot correlates a macroscopic property, i.e., the relative density, with the samples' microstructure. Furthermore, it highlights that keyholes formed as the energy density increases and the reason of this lies in the mechanisms of keyhole formation (Section 3.3.1).

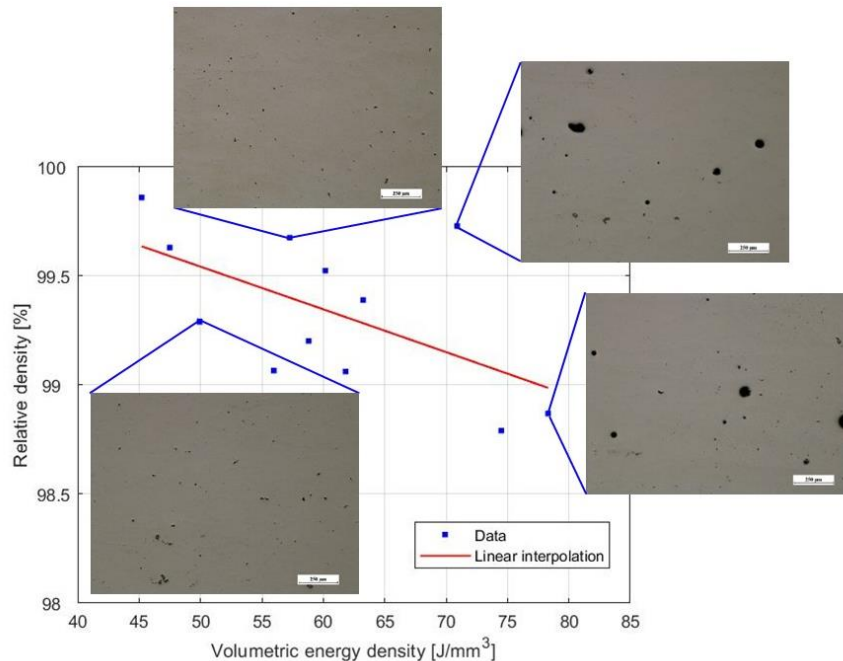


Figure 32 Relative density depending on volumetric energy with optical microscopy images

Afterwards, samples are subjected to chemical etching to show the melt pools. Starting with Figure 33, a magnified view of the melt pool shape of sample P is shown. A finer grain structure is observed inside, while a coarser grain is formed along melt pool borders due to the gradient change of the solidification rate. Even if not visible from Figure 33, the microstructure of AlSi10Mg that forms during the SLM process is characteristically composed by Al matrix grains surrounded by a fibrous Si network.



Figure 33 Melt pools, magnified view sample P

Since the EOSM290 used for the specimen production rotates the laser scan direction by 67° after every deposited layer, the result is an articulated pattern of interwoven melt-pool width and overlap on a section along the z direction that is through the built part. This structure is schematically and experimentally illustrated in Figure 34 with an optical micrograph of an etched sample, in this case cube J.

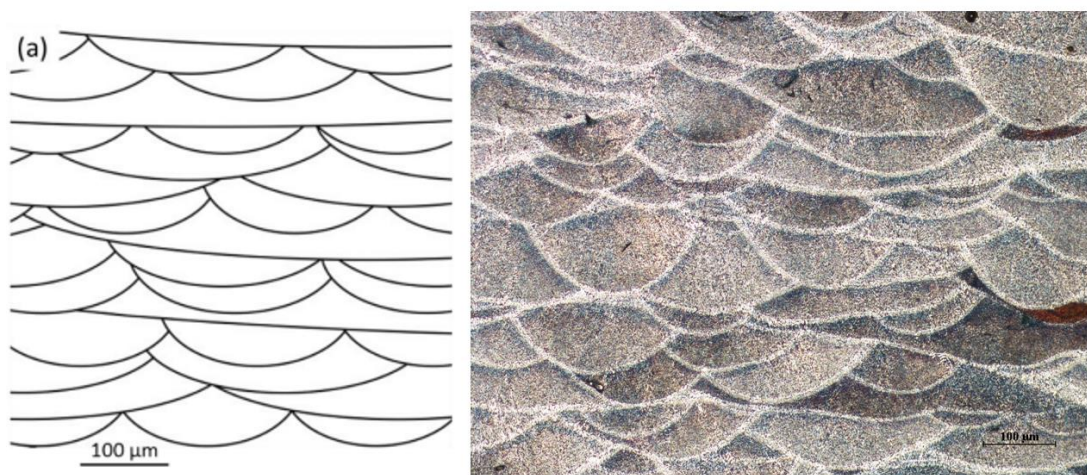


Figure 34 Melt pools schematic illustration [18] left side, experimental of sample J right side

According to the work done by M. Krishnan et al in [19], increasing the hatch spacing, the melt pools overlapping reduces. This effect is nevertheless limited by the scanning strategy adopted and by the slightest difference between the two hatch spacings used for this case study. As a confirmation, Figure 35 shows a comparison between the melt pools of two samples, Q and S,

processed with the same laser power of 352 W and scan speed of 1050 mm/s but different hatch spacing and the difference in melt pools overlapping is hardly noticeable.

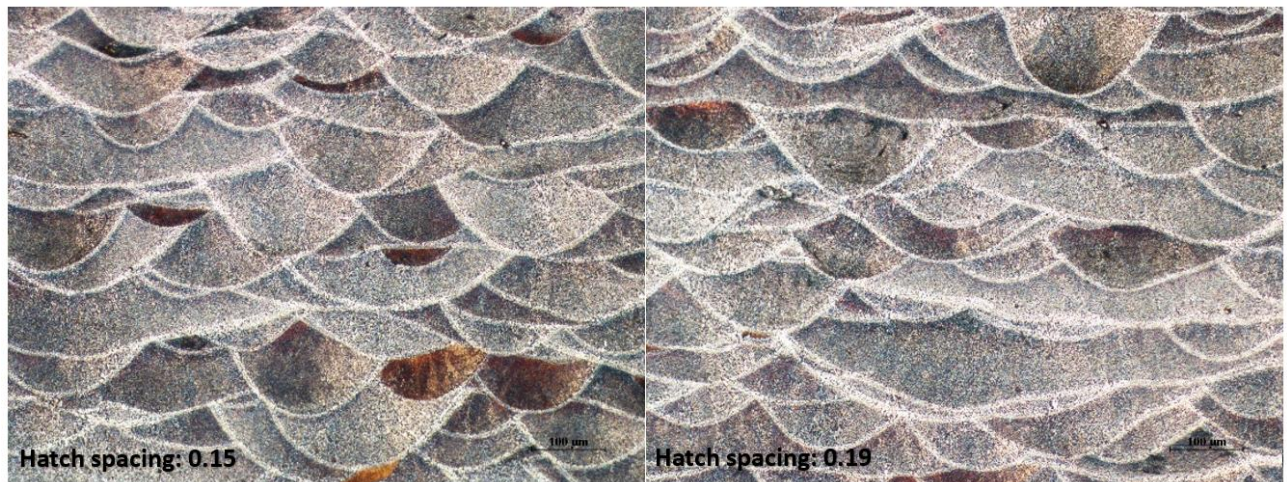


Figure 35 Melt pools of sample Q left side and R right side

3.3.3 Concluding remarks

In a complex process such as the SLM process, the performance and outcome are very often affected by a group of variables rather than a single one. Therefore, the need to identify, investigate and prioritize the influencing SLM parameters and their interdependencies to ensure high process stability and reproducibility is of paramount importance.

The results obtained in the mechanical characterization of cubes for density and hardness are considered eligible. Indeed, the process parameters used for their production are within the operating window defined by the hatched red area in the graph of Figure 17.

Thanks to the high efficiency of the SLM process and the high solidification rate the material experiences, it is possible to obtain higher HV values of the part if compared to casting.

To achieve favorable microstructure and consequently a part with high mechanical properties, the optimal parameters are selected with the objective of increasing the density of the part, which is mainly responsible for the properties of the tested material. According to Table 6, sample H is the one that shows the highest relative density value, 99.86%. If Table 7 is considered, this sample also has one of the highest values of Vickers hardness, 130 HV, and it has a volumetric energy density of 45.21 J/mm³ which is well below the limit above which keyholes occur, according to Figure 32. For these reasons, the process parameters selected for the next step of the project, together with the corresponding volumetric energy density, are the ones resumed in Table 8.

<i>Process parameter, sample H</i>	<i>Unit of measurement</i>	<i>Value</i>
<i>Laser power</i>	W	335
<i>Layer thickness</i>	mm	0.03
<i>Scan speed</i>	mm/s	1300
<i>Hatch spacing</i>	mm	0.19
<i>Volumetric energy density</i>	J/mm ³	45.21

Table 8 Final process parameters selection

4. Topology optimization of the part

This section is dedicated to the optimization of the ICE piston in AlSi10Mg with static FEM analyses with the Altair Inspire® software.

Tensile tests are carried out on dogbones samples to assess the mechanical properties of the AlSi10Mg alloy, i.e., the tensile strength, Young modulus and ultimate tensile strength (UTS), that the software considered as the input for the simulation. Thereafter, a FEM analysis is carried out on the baseline configuration of the piston (Section 2). Finally, a topology optimization is carried out and three different designs of the piston are obtained.

4.1 Tensile test

Once the optimized parameters that give maximum density are identified, tensile tests are performed on apposite manufactured samples.

Five tensile specimens are built along the xy plane with process parameters reported in Table 8 with the EOS M290 and the same scanning strategy used for the cubes. The specimen conforms to the ASTM E8/E8M – 13a Standard that is the Test Methods for Tension Testing of Metallic Materials [20], its CAD representation is reported in Figure 36 with a 3D view and its corresponding drawing, dimensioned in mm.

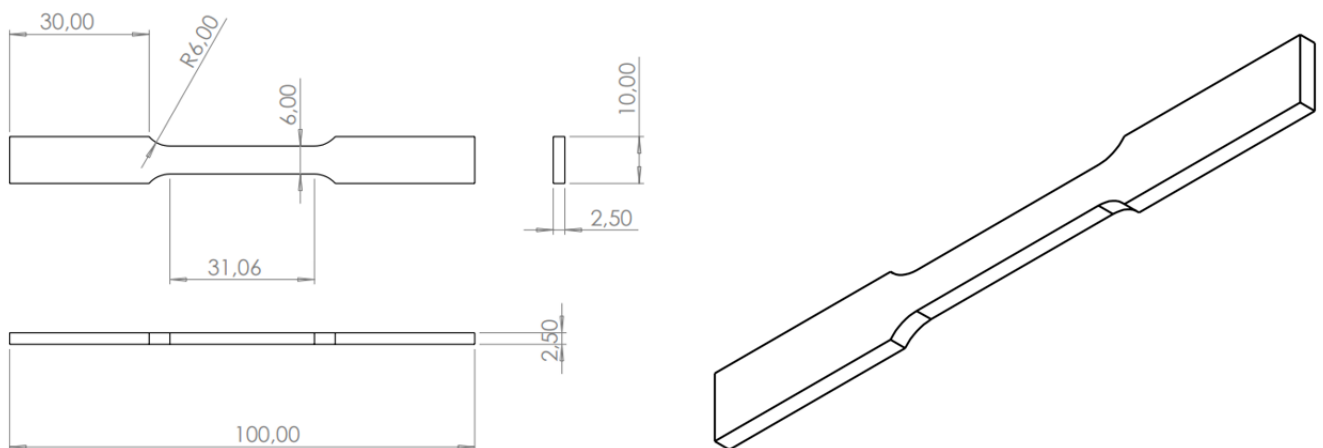


Figure 36 Rectangular Tension Test Specimen, quotations in mm

More in detail, this ASTM standard covers the tension testing of metallic materials in any form at room and constant temperature. Specifically, this method provides the determination of yield strength, yield point elongation, tensile strength, elongation, and Young Modulus [20]. This characterization is done with a static tensile test. The tensile tests are performed on the

specimens in the as-built condition i.e., no heat treatments nor surface finishing is applied. The stress-strain curves obtained for each specimen are reported in Figure 37.

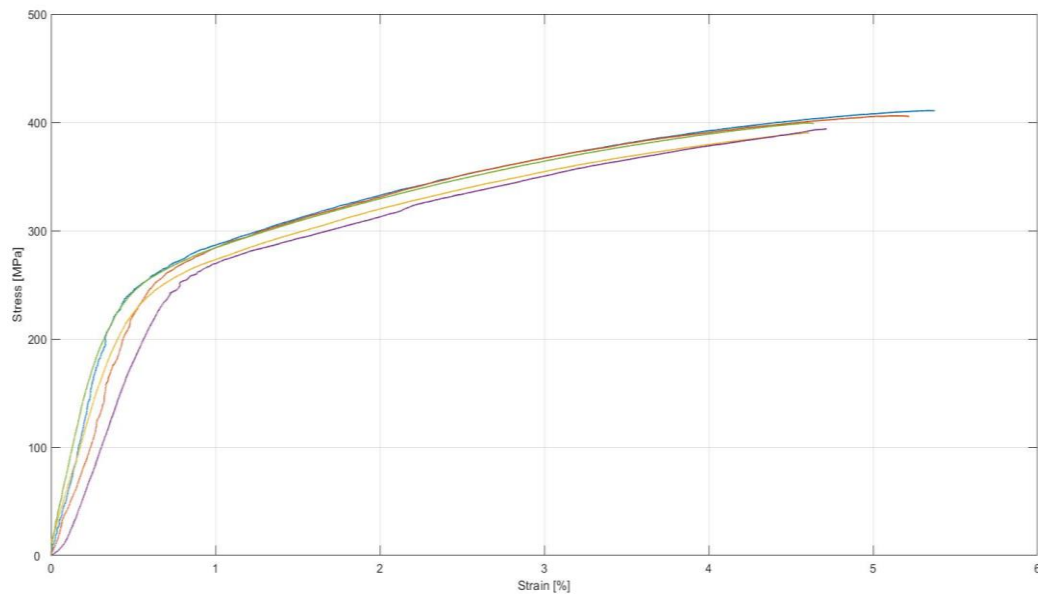


Figure 37 Tensile tests on dogbone specimens: stress-strain curves

The results of the tensile tests data for each dogbone specimen are resumed in Table 9. The Yield stress is assessed with the offset method described in ASTM E8/E8M – 13a Standard that is the Test Methods for Tension Testing of Metallic Materials [20], i.e., with an offset of 0.2%. The graphic representation of this method is illustrated in Figure 38 with the tensile curve of sample 5 used as a reference.

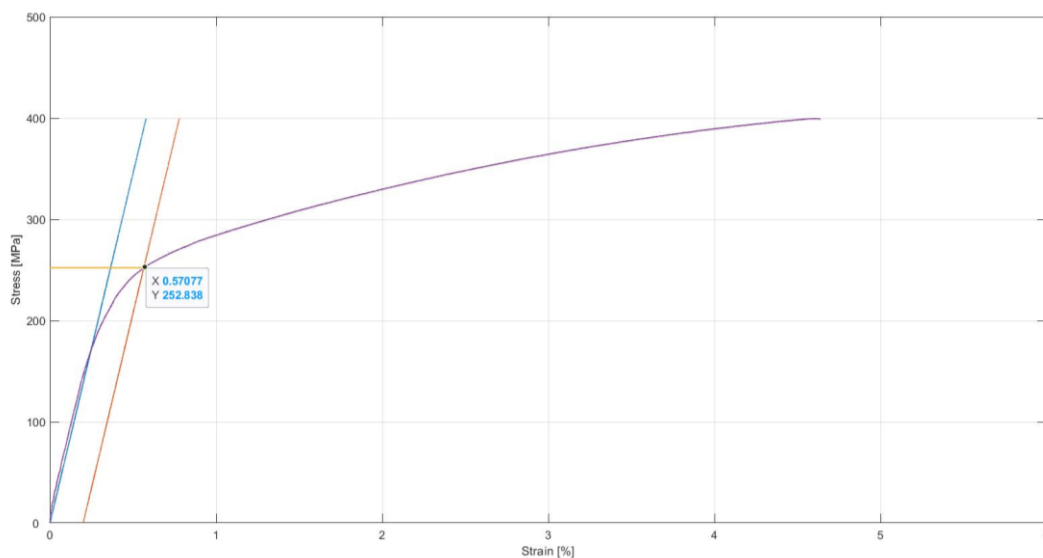


Figure 38 Yield stress evaluation - Test sample 5

	<i>Unit of measurement</i>	<i>Test 1</i>	<i>Test 2</i>	<i>Test 3</i>	<i>Test 4</i>	<i>Test 5</i>
Young Modulus (E)	GPa	68.06	55.95	50.14	43.34	69.03
Yield stress (YS)	MPa	259.05	254.17	252.31	245.90	252.84
Ultimate tensile strength (UTS)	MPa	410.87	406.00	390.25	394.01	399.29

Table 9 Results from tensile test data analysis

The evaluation of the Young Modulus and the relative elastic range is performed considering a linear fitting curve for the data in the elastic range. The results obtained from the tensile tests are in agreement with the literature data for the AlSi10Mg alloy produced with SLM in the as-built condition [21] except for the value of Young's modulus, which is slightly lower on average than the expected value of 71 ± 10 GPa. This discrepancy between the values obtained and those stated for the alloy may be due to several factors. The specimens used had a slight curvature probably due to the separation procedure from the EOS M290 platform, this may have influenced the test itself. In addition, issues related to correct strain detection by the machinery used for the test are not excluded. Additional analysis of this divergence would be required especially for the elastic modulus; however, this is not the objective of this study. This is why the investigation proceeds by considering only the two optimum tests, i.e., Test 1 and Test 5, which guarantee, for the optimized process parameters considered, the expected mechanical properties for AlSi10Mg.

To summarize, the data used for the FEM analysis of the part with AlSi10Mg alloy that is discussed in the next section, are provided in Table 10.

E	ν	YS	UTS	α	ρ	λ
GPa	-	MPa	MPa	K ⁻¹	Kg/m ³	W/(m·K)
68.545	0.33	255.95	405.05	$21 \cdot 10^{-6}$	2680	170

Table 10 AlSi10Mg - Mechanical properties

4.2 FEM analysis on the AlSi10Mg part

Considering the part presented in Section 2 with the same loads and constraints, a Finite Element model of the piston can be created, by considering AlSi10Mg as constitutive material. Also in this case, a static analysis of the investigated part in a steady state is carried out with the commercial software Altair Inspire® considering the same element size of 0.8 mm for the

model. The baseline configuration analyzed in this section has a volume of 135081 mm³ and a mass of 0.36202 kg.

The results are shown in Figure 39, which shows the safety factor distribution. The minimum detected safety factor is 2.953, which ensures the reliability of the part for these load cases.

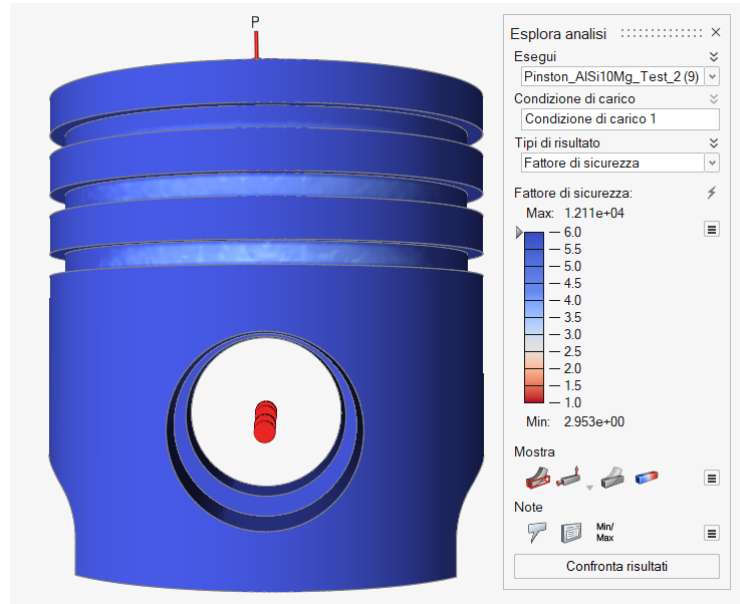


Figure 39 Factor of Safety - Baseline piston in AlSi10Mg

The Von Mises stress distribution reported in Figure 40 ranges from a minimum value of $2.111 \cdot 10^{-2}$ MPa up to a maximum value of $8.654 \cdot 10^1$ MPa. These values are slightly higher if compared to the ones obtained in the previous case for the part in AlCu4MgSi alloy. Also in this case, stresses are distributed almost homogeneously over the whole component and the most stressed areas correspond once again to the internal edge of the piston, at the connection of the top part of the component with the lateral surfaces.

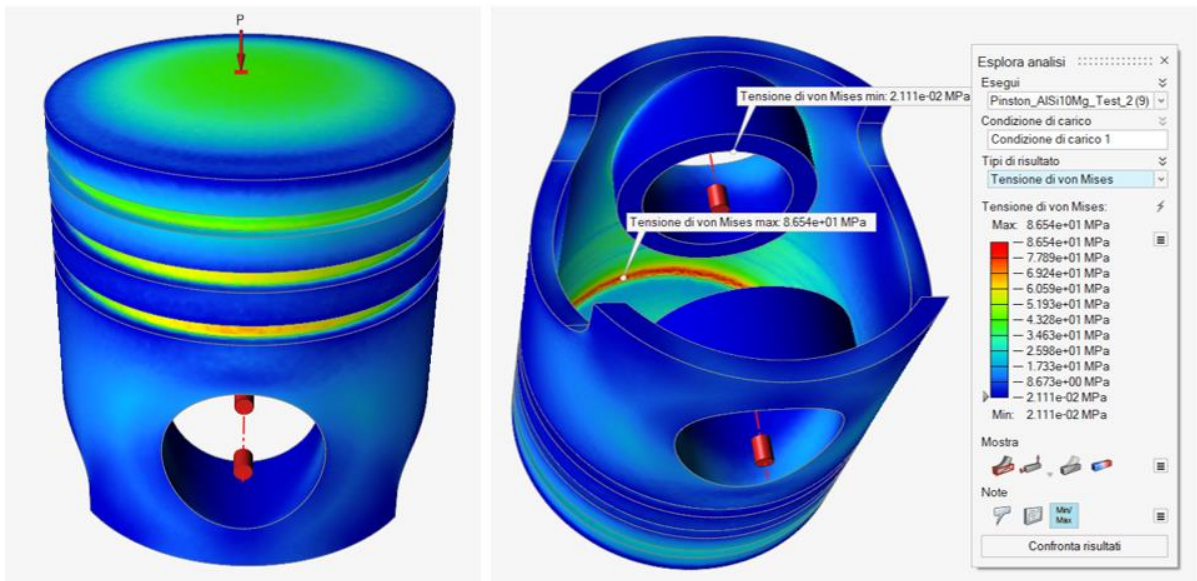


Figure 40 Von Mises Stress - Baseline piston in AISi10Mg

The last result analyzed is the distribution of tension and compression stresses on the part, shown in Figure 41. Again, the distribution and the values of tension and compression are similar to the ones presented for the baseline piston in Section 2.

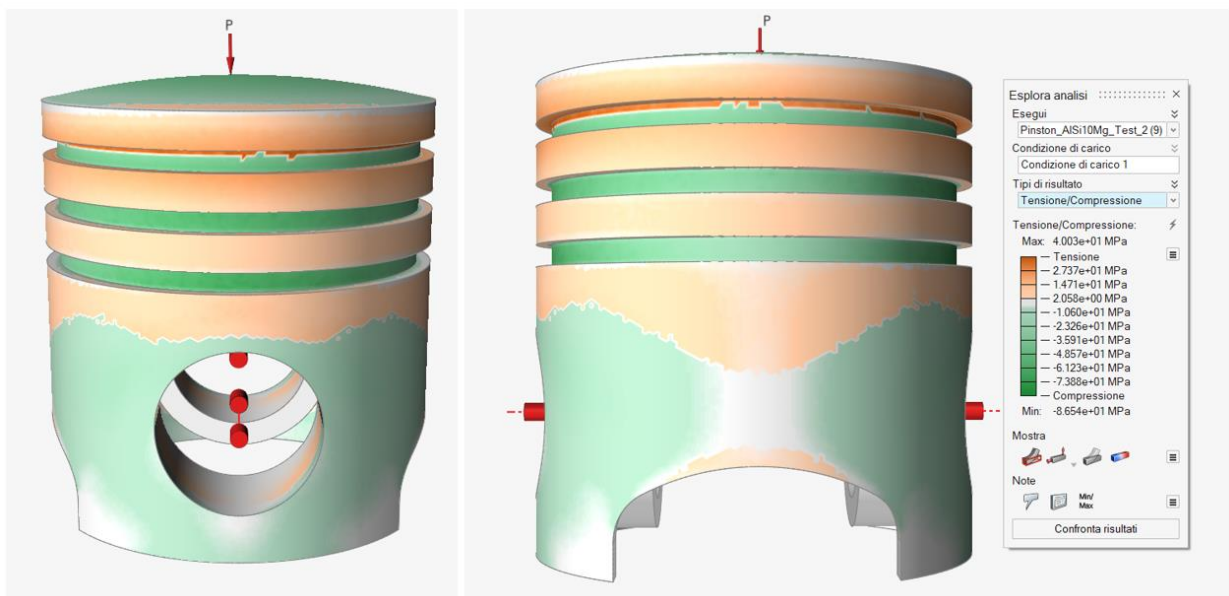


Figure 41 Tension/Compression Stress - Baseline piston in AISi10Mg

This analysis evaluates the performances of the part in the operating conditions, and, in this case study, it also represents the starting point for the design optimization of the component presented in the next section.

4.3 Design optimization

The design optimization is carried out starting from the suggested topology in Altair Inspire®. Structural topology optimization is an optimized arrangement of material in a defined work domain, that eliminates the volume that is not necessary for withstanding the applied loads. Topology optimization algorithms provide the structural layout that best transfers loads within the part starting from an original configuration. It is often used to generate an initial layout of the structural system, which is then refined depending on the specific application to satisfy the operating conditions.

As a first step, the work domain has to be identified: it corresponds to the part to be optimized and it is divided into design and non-design space. The first one constitutes the volume in which the material can be removed while the latter is the volume in which the software must not act. The definition of the non-design space is important because it includes the portions whose modifications can compromise the component operation. In this case the volume included in the non-design space is composed by both internal surfaces of the piston holes, the piston top and the top land because they must comply with stricter tolerances. In Figure 42 the non-design space is highlighted in light blue.

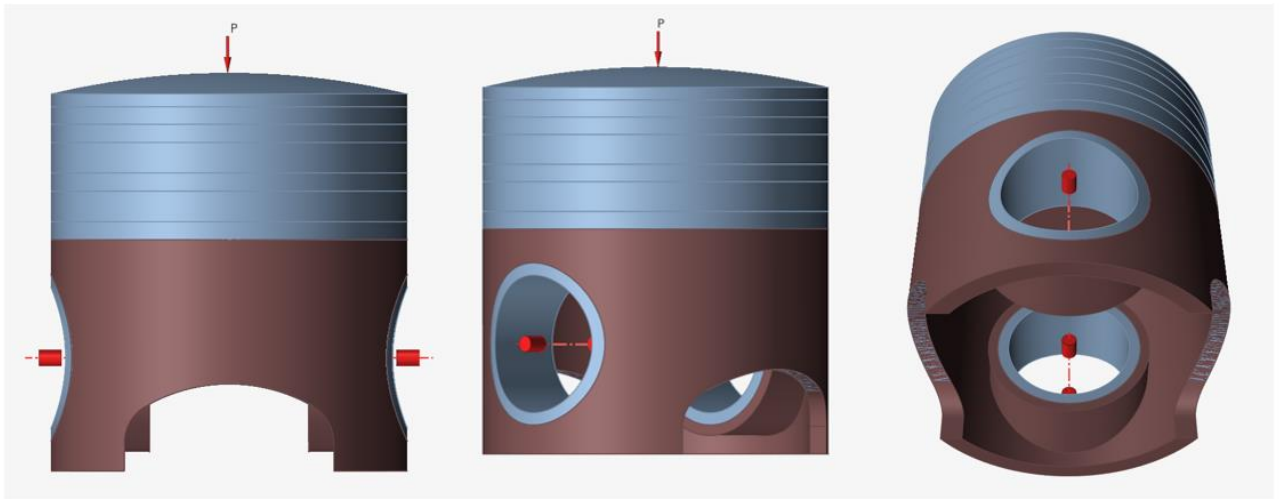


Figure 42 Design and non-design space of the baseline configuration

Different types of optimizations are available in Altair Inspire, including topology, topography, gauge, and lattice optimization. In this case study the interest is on topology optimization, which provides the optimized material distribution by removing unneeded material from the design spaces, creating the lightest structure capable of withstanding the forces applied to the part. The objective of this analysis is to maximize the stiffness of the component while trying to

achieve a lower mass than the starting value which is 0.36202 kg. A mass target is required to start the simulation and in this case is given 85% of the initial mass. The optimized configuration obtained from the software is presented in Figure 43.

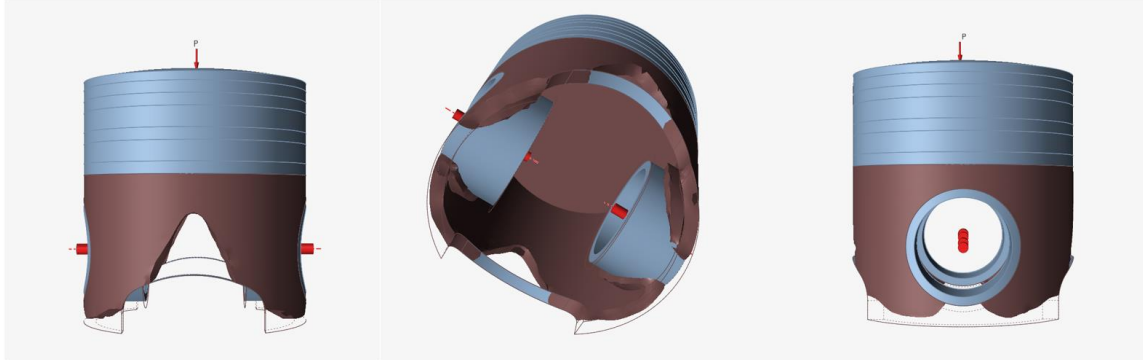


Figure 43 Topology optimization of the part

The next step, considering this optimization, is the rebuilding of the part. It has to be modified with smoother removal of volume fraction to ensure continuity and regularity to the part surfaces. Considering not only the piston functionality but rather the mechanism as a whole, volume reductions up to 15% of the part, as suggested from the software, are not expected for the final design since the aim is to ensure the component's performance under the most critical load condition. CAD models of the three different designs analyzed in this case study are presented in Figure 44.

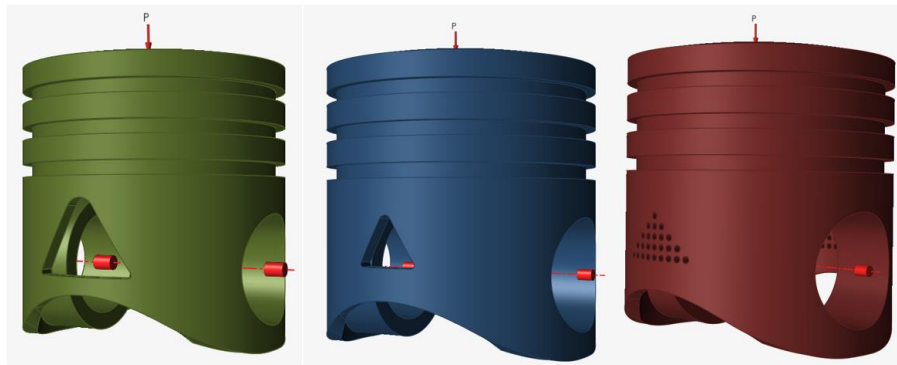


Figure 44 From left to right: 1st Design, 2nd Design and 3rd Design proposed

The common feature of these three configurations is the lower part of the skirt that is rounded in comparison with the base configuration. In addition, in every scenario, a part of the volume is removed from both the lateral surfaces of the piston. In the first two cases, the volume is removed from both the lateral surfaces of the piston with a triangular hole of different sizes, while in the third with a series of small circular holes, always following the pattern of the optimization presented in Figure 43.

These designs are now individually analyzed with FEM analysis as a first validation in terms of mechanical performance compared to the baseline configuration. The aim is to preserve the functionality of the part not compromising its performance while reducing the total mass of material used for it. The FEM analysis carried out in this study is a static analysis, as for the baseline configurations, to evaluate the safety factor, the Von mises stress and tension and compression distribution on the part. Loads and constraints are the same used for the baseline configurations in Sections 2 and 4.2.

4.3.1 1st Design

The first design suggested is reported in Figure 45. It is characterized by the rounded profile of the lower part of the skirt and a hole in the lateral surface of the piston which follows the pattern of the optimization presented in Figure 43 of the part. The hole has a triangular shape with smoothed edges to prevent residual stresses, stress concentration and potential failures. Thanks to these modifications of the CAD of the part it is possible to obtain a volume of 127768 mm³ and a total mass of 0.34242 kg which correspond to the 94.59% of the initial volume and mass of the piston.

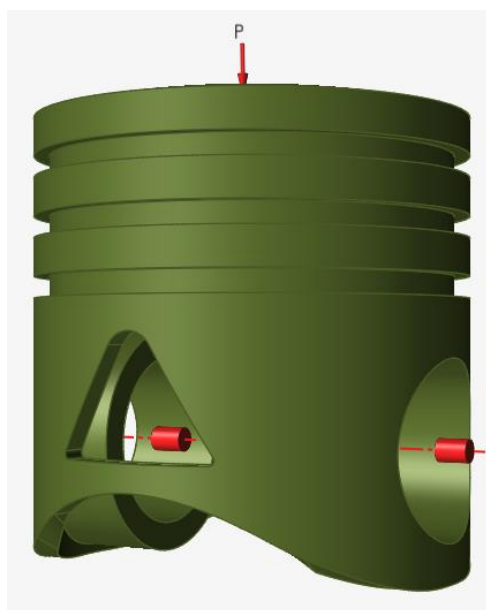


Figure 45 1st Design

Starting from the evaluation of the safety factor, from Figure 46 it is evident that some regions are at risk of failure because the SF is below 1.

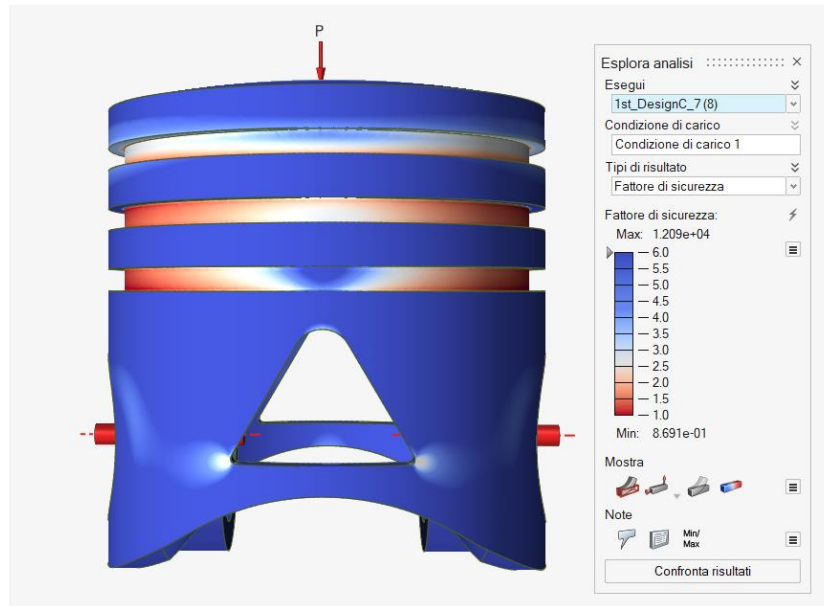


Figure 46 Factor of Safety - 1st Design in AISi10Mg

In Figures 47 and 48 are presented the Von mises stress distribution is shown, together with the compression/tension state of the part. With respect to the baseline configuration, compression and tension stresses have increased: indeed, due to the optimization process, the piston must also support the stresses previously withstood by the material that have now been eliminated.

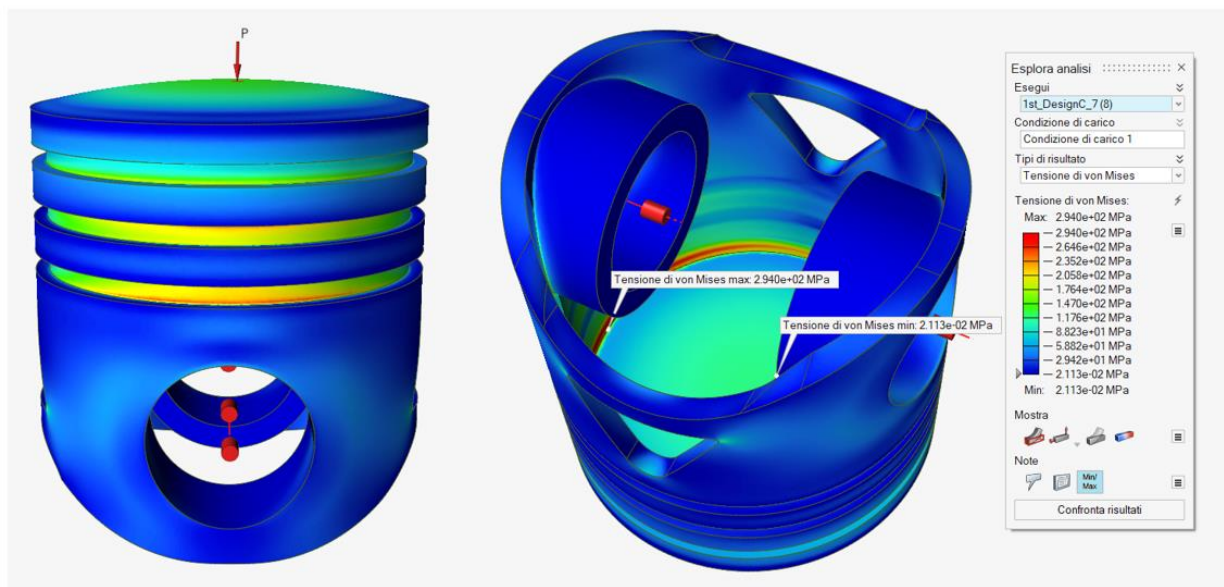


Figure 47 Von Mises Stress - 1st Design in AISi10Mg

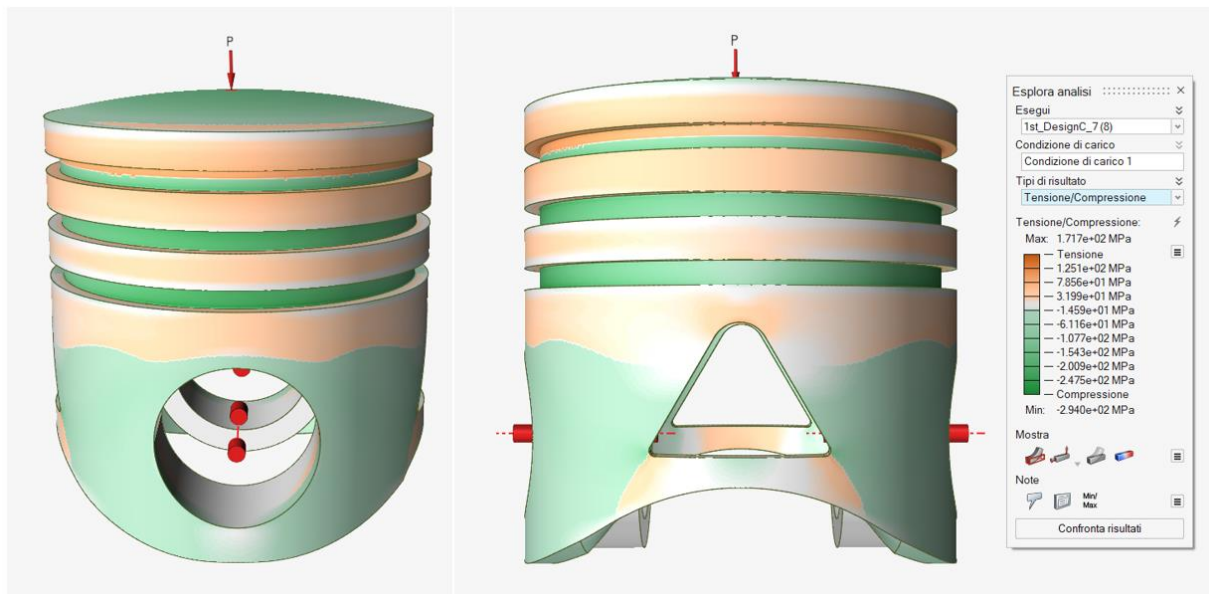


Figure 48 Tension/Compression Stress - 1st Design in AISi10Mg

4.3.2 2nd Design

The second design is similar to the first one, but the side triangular hole is different. Its CAD model is reported in Figure 49. This design of the part has a mass of 0.34916 kg and a volume of 130282 mm³ which corresponds to 96.45% of the mass and volume of the baseline piston.

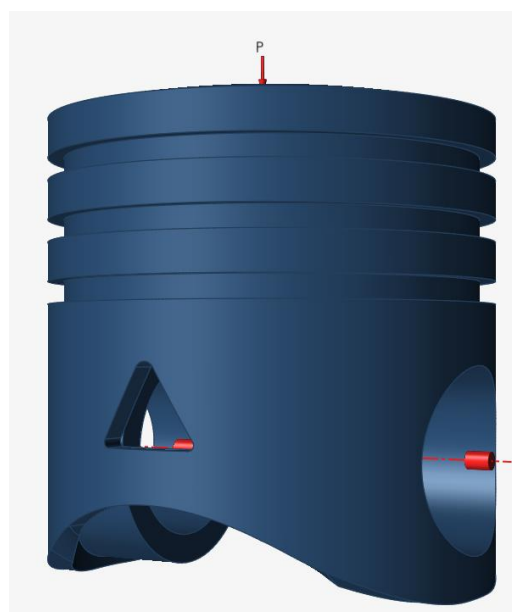


Figure 49 2nd Design

The FEM analysis starts with the SF of the part reported in Figure 50. The minimum value is 1.21 in the piston ring region, which turns out to be again the most critical area.

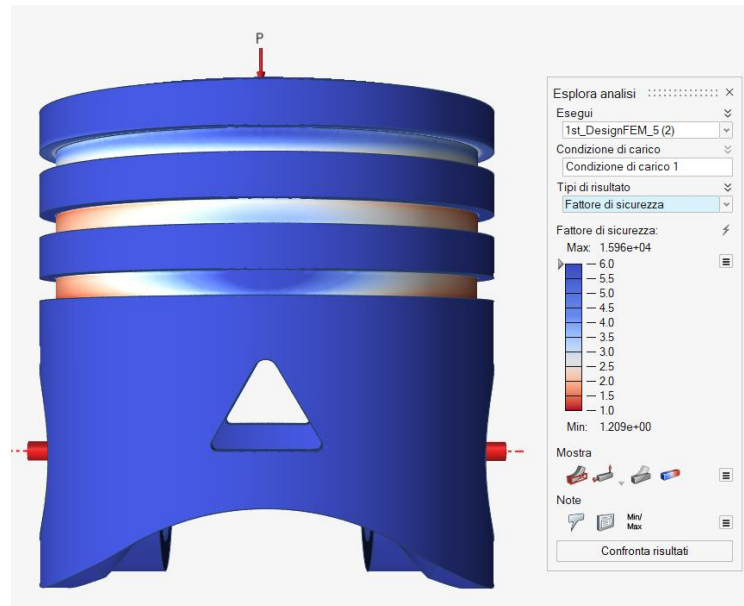


Figure 50 Factor of Safety - 2nd Design in AISi10Mg

Von mises stress analysis and compression and tension state of the model are shown in Figures 51 and 52.

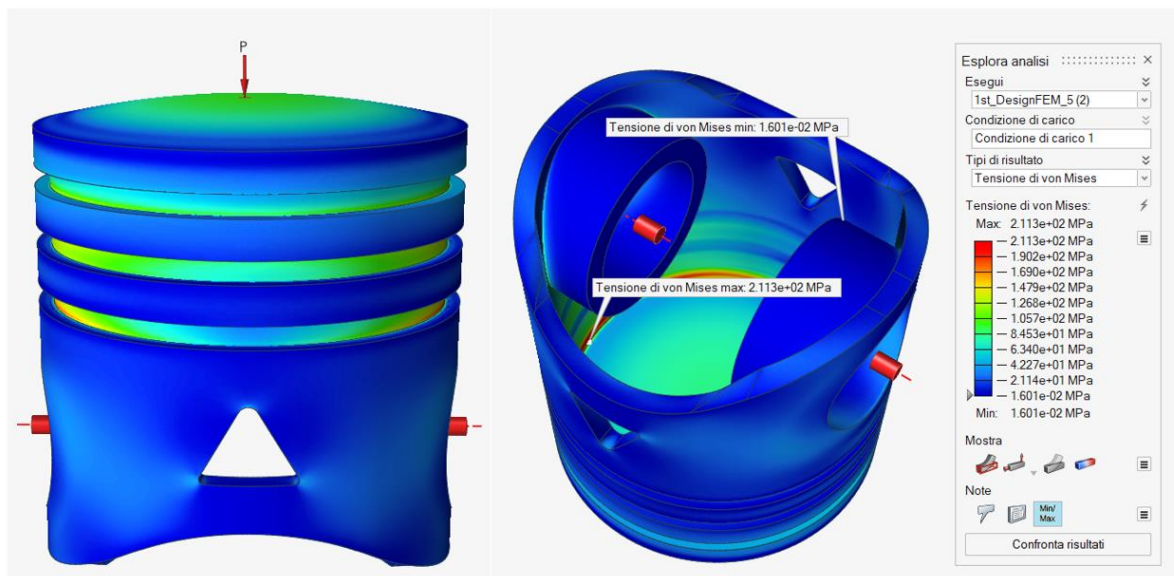


Figure 51 Von Mises Stress - 2nd Design in AISi10Mg

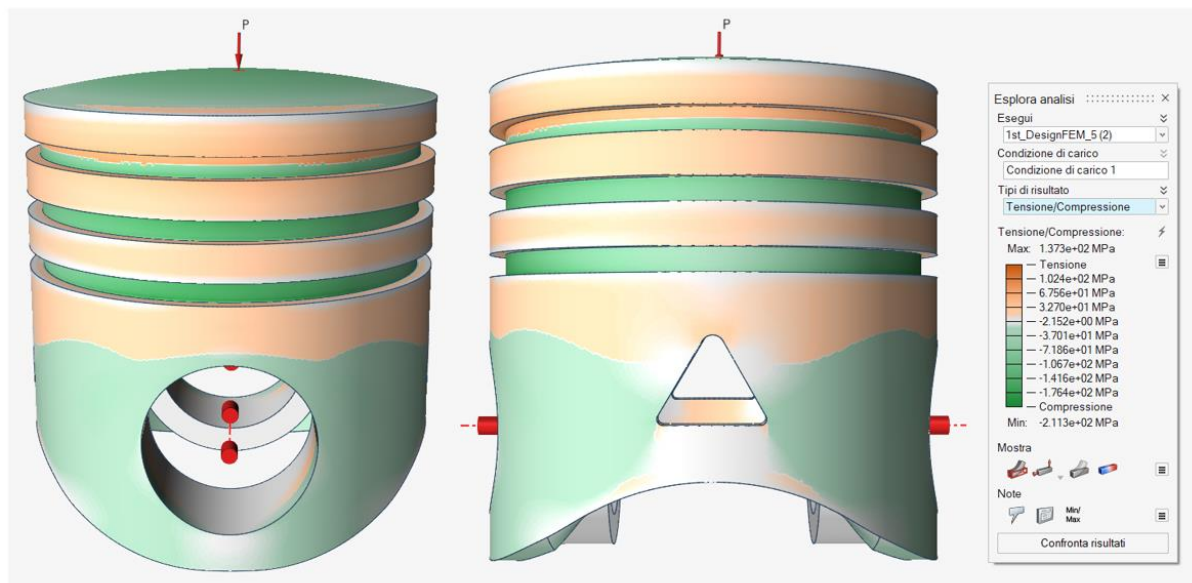


Figure 52 Tension/Compression Stress - 2nd Design in AISi10Mg

4.3.3 3rd Design

The last configuration is characterized by multiple circular holes within a triangular shape. The CAD model is shown in Figure 53.

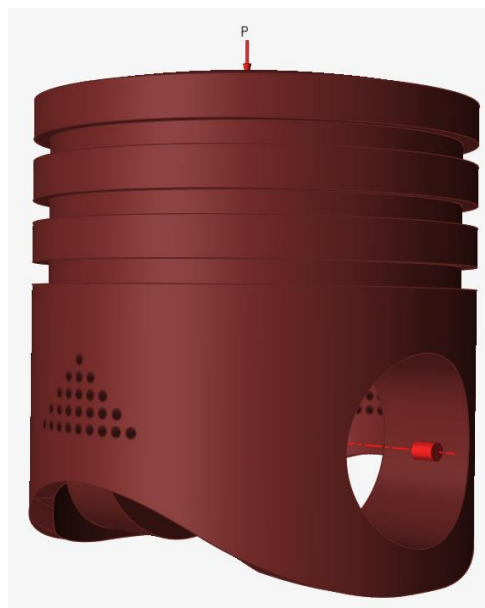


Figure 53 3rd Design

In this case the component has a mass of 0.35124 kg and a volume of 131000 mm³ which is the 97% of the initial one. The removal of material in this configuration limits the reduction of the mass but, on the other hand, ensures a better stress distribution. This can be found in the results

of the FEM analysis shown in Figure 54, with the SF that has a lower limit of 2.04, close to the one of the baseline configuration.

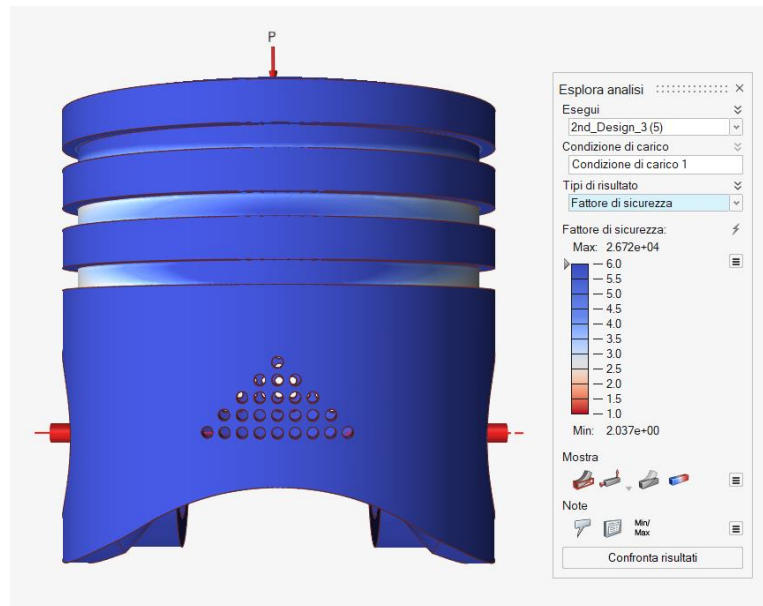


Figure 54 Factor of Safety - 3rd Design in AISi10Mg

Von mises stress analysis and compression and tension state of the model are proposed in Figures 55 and 56.

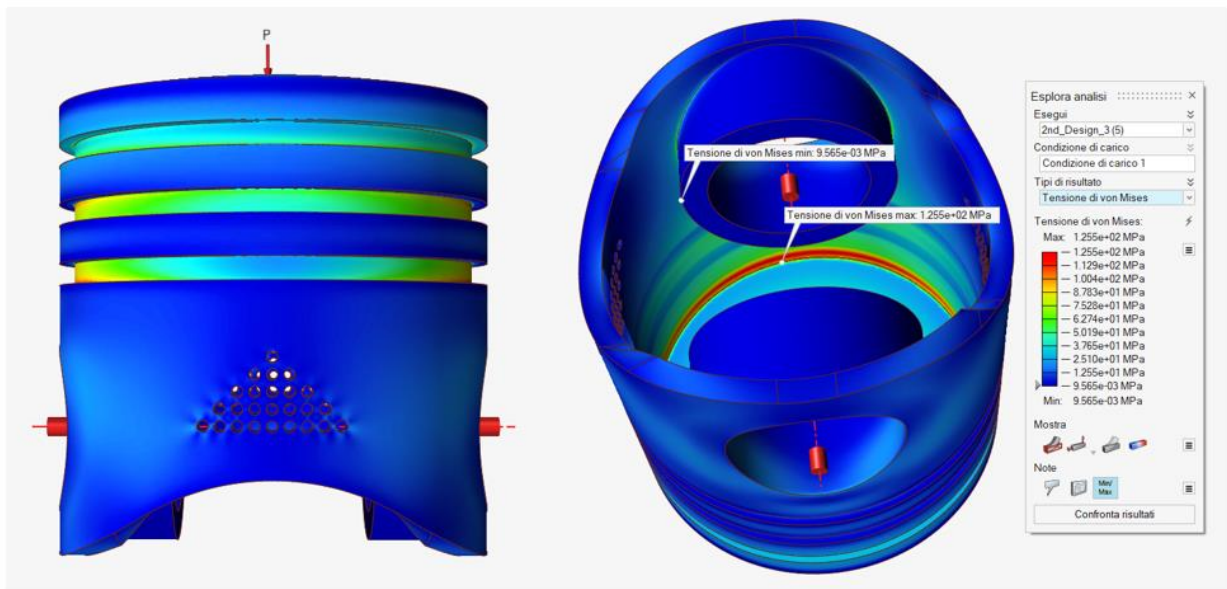


Figure 55 Von Mises Stress - 3rd Design in AISi10Mg

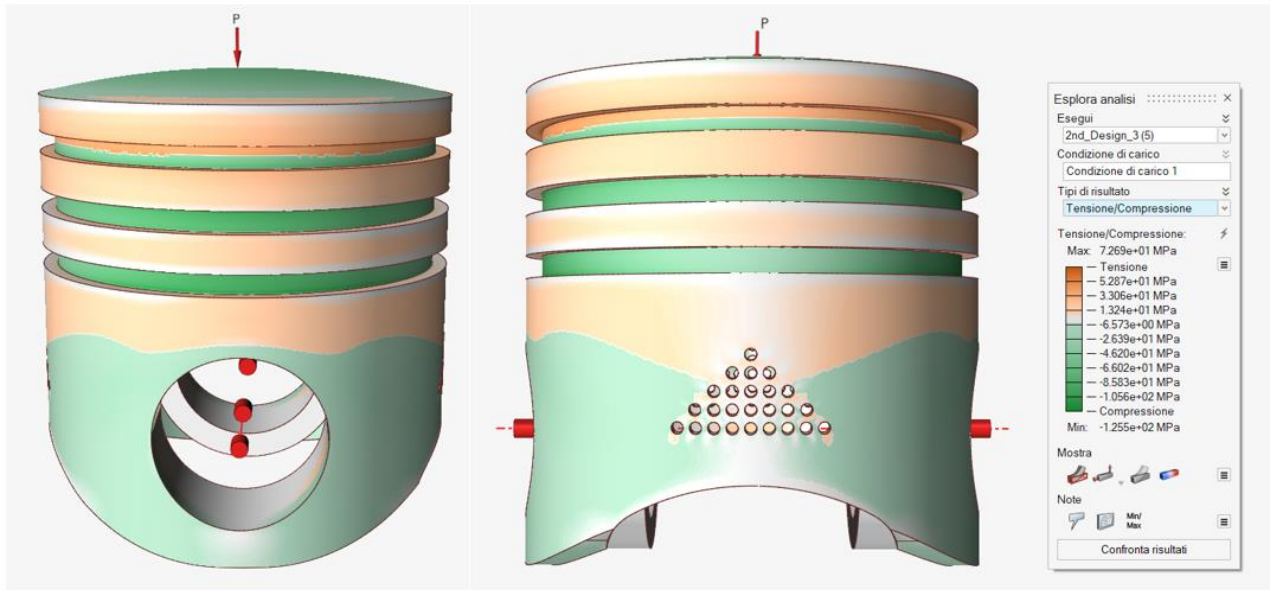


Figure 56 Tension/Compression Stress - 3rd Design in AlSi10Mg

4.4 Final design choice

The final choice of a design over the other two is carried out on the basis of the results of the FEM analysis to ensure the component's performance under the most critical load condition. Table 11, summarizes the main results of the FE analysis and the reduction in terms of mass for each configuration with respect to the baseline.

	Unit of measurement	Baseline	Baseline	1 st design	2 nd design	3 rd design
Material		AlCu4MgSi	AlSi10Mg	AlSi10Mg	AlSi10Mg	AlSi10Mg
Von Mises stress min	MPa	$3.77 \cdot 10^{-3}$	$2.11 \cdot 10^{-2}$	$2.11 \cdot 10^{-2}$	$1.60 \cdot 10^{-2}$	$9.57 \cdot 10^{-3}$
Von Mises stress max	MPa	52.0	86.54	294.0	211.3	125.5
SFmin		5.23	2.95	0.87	1.21	2.04
Tension	MPa	29.50	40.03	171.7	102.4	72.69
Compression	MPa	-52.03	-86.54	-294.0	-211.3	-125.5
Volume	mm ³	135081	135081	127768	130282	131000
Mass	Kg	0.37688	0.36202	0.34242	0.34916	0.35124
Mass reduction	%	-	-	5.41	3.55	3

Table 11 FE analysis: Comparison of proposed designs

As can be seen from the last row of Table 11, the first solution, 1st Design, is the one that provides the greatest reduction in terms of material among the three. However, the FEM analysis shows for this option a minimum safety factor of 0.87, being not safe. For this reason, this solution is to be excluded.

The second option, 2nd design, allows a lower volume reduction since the triangular hole is smaller than in the previous case. As expected, the maximum stresses detected in the part are higher with respect to the baseline configuration but still acceptable with a safety factor of 1.21. This design can be still taken into account for the above-mentioned reasons.

In the last optimization, 3rd design, the reduction in terms of mass corresponds to 3% which is the lowest among all the proposed solutions. Nevertheless, considering the stress distribution among the part, this design has a maximum Von Mises stress of 125.5 MPa and a safety factor of 2.04 which is a value close to that of the baseline configuration in AlSi10Mg (2.95) that is acceptable. Furthermore, taking into account the entire process of part manufacturing with selective laser melting, this design is the only one among the proposed that does not require the manufacturing of supports in the side hole of the piston. For the realization of 1st and 2nd designs with the SLM technique, support structures should be manufactured during the AM process of the part, given the considerable size of the triangular hole that would otherwise collapse on itself. This problem does not arise in the 3rd design because the smaller size of the holes allows them to be manufactured without the aid of the supports.

Considering the entire optimization process of part realization with SLM and not focusing only on mass reduction, the last solution results to be the best option for this case study. The discussion from now on will then focus on the next steps necessary for manufacturing of the piston considering the CAD of the 3rd design.

5. Build process

This paragraph is dedicated to the steps to be followed for printing the part and to the post-process required for optimizing its performance. Like any manufacturing process, also Additive Manufacturing follows a specific workflow, which is schematized through its main 9 steps in Figure 57.

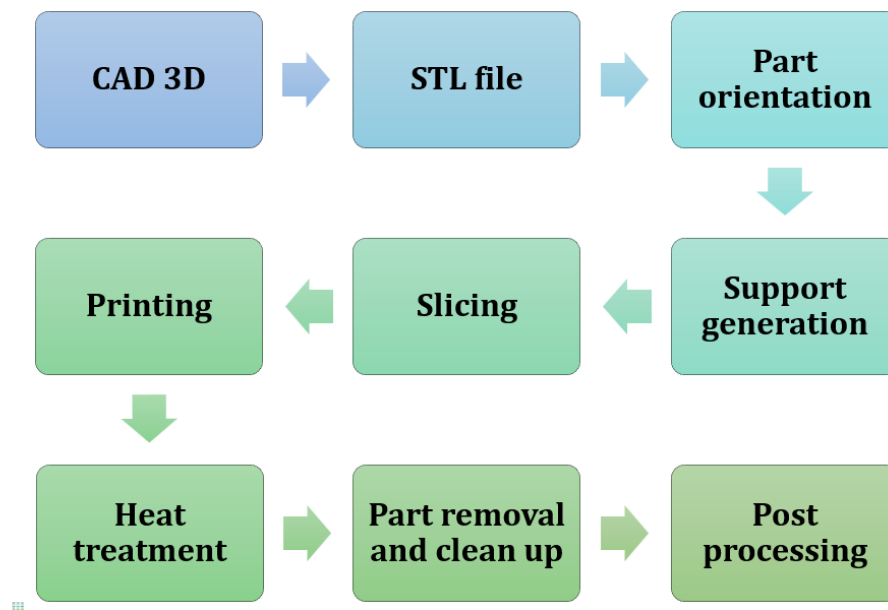


Figure 57 AM workflow for part production

The 3D CAD model of the part is the starting point of the process. For this case study it is the optimized configuration of the piston under study shown previously in Figure 53.

The CAD file is converted to the STL format, which, as mentioned in Section 3, represents the universal standard of mathematical models for additive manufacturing. The STL file is exported either directly to the machine or into dedicated software that allows further work on it, e.g. allowing the evaluation of the orientation of the part and its supports, if needed.

Part orientation in the building volume of the machine is a crucial step of the process because it determines the quantity and the location of the supports and the type of slicing. Consequently, this influences the quality of the printed part, the printing time, and the mechanical properties, as AM is an anisotropic process. Support structures are used mainly for two reasons:

- Anchor the component to the working platform, allowing for its subsequent removal.
- Support the parts to be manufactured, preventing collapses and deformations.

Support structures may also have other functions, such as distributing heat over the component to improve thermal distortions due to the high temperatures involved.

Despite the importance that supports have, they still represent material waste for the production process, which during the printing phase has to be created and in later stages has to be removed. For this reason, it is essential to properly orient the component in the building chamber volume to minimize supports, precisely to keep a low printing and post-processing time and cost. These two phases, part orientation and support generation are strictly correlated for the above-mentioned reasons. For this case study, to better exploit the geometry of the part, the piston is oriented so that the printing process starts from its convex top part toward the housing of the pin. In this way, since the base of the part is denser, the overall printing process requires less support structures. This approach promotes the grain growth along the direction in which the main applied stresses are oriented. This part orientation with its supports is shown in Figure 58.

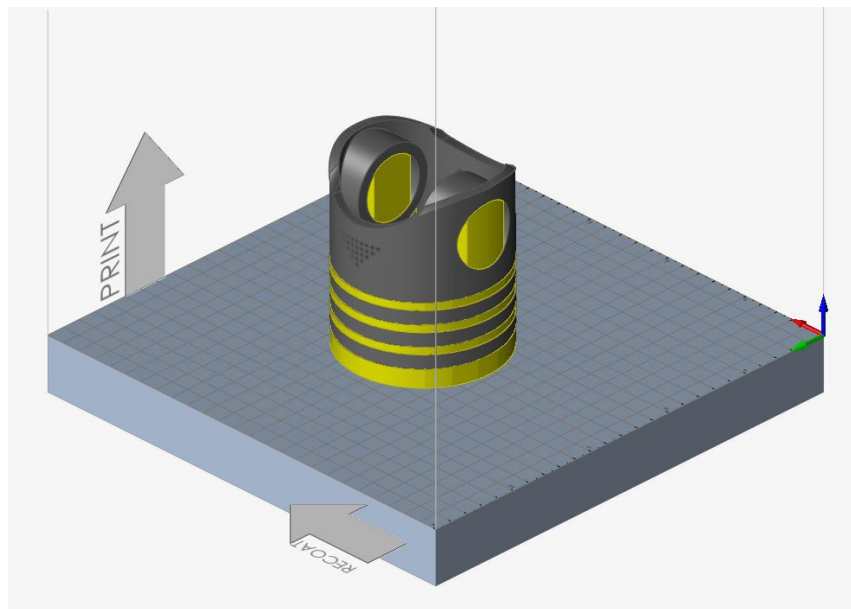


Figure 58 Building platform placing of the part with supports

Considering the support generation proposed, the production of piston rings by AM might not be the best option for this part since the mechanical removal of the support structures could affect the surface quality of a so narrow area. This is why it has been chosen to produce the component at first with a plain side surface and manufacturing the grooves after the AM process with a traditional subtractive process. Part orientation without rings is shown in Figure 59.

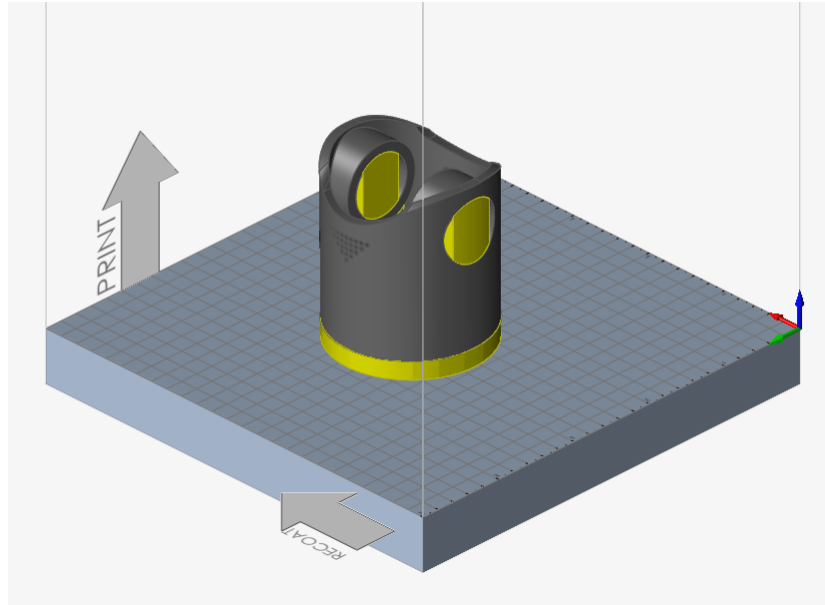


Figure 59 Building platform placing of the part with supports without rings

The next step, after part orientation and support generation, is the slicing phase. It consists in subdividing the component into sections of thickness equal to Δs , which are then realized during the printing process. This procedure is schematized in Figure 60 and involves a succession of planes parallel to each other and perpendicular to the direction of growth of the component. As can be noticed, also this phase depends on the choice of part orientation inside the machine building volume.

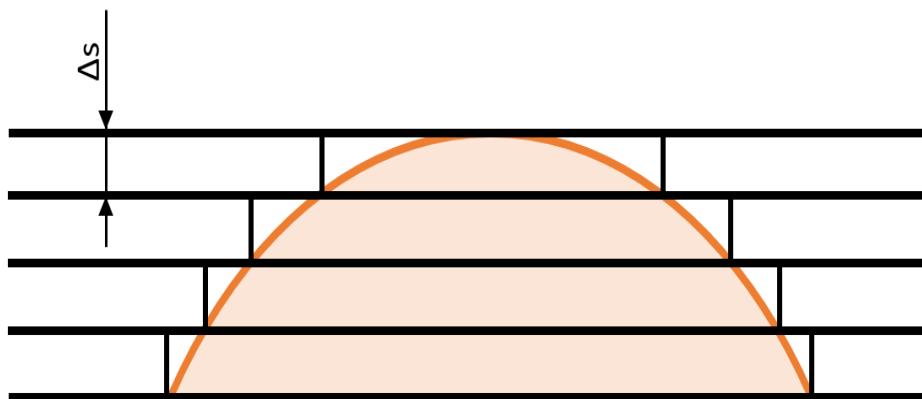


Figure 60 Slicing, schematic representation

The Δs values depend on the AM machine and the lower these values are kept, the better the surface quality is, because slicing is associated with the "staircase" error and with a stepped surface. However, the printing time and the .stl file dimensions increase by reducing the Δs value. Accordingly, a trade-off should be found. In this case study, the piston is printed with its

axis perpendicular to the building platform to minimize the typical stair-stepping appearance. The slicing procedure is implemented in the Altair Inspire software.

After these steps, the component is ready to be printed and a simulation of the manufacturing process is run. During the printing phase, the component takes shape starting from the stratification of the different layers. Altair Inspire allows selecting the SLM machine used in this study, i.e., the EOS M290 AM machine, with all the optimized process parameters that were reported in Table 8. For the printing operation, two main results are analyzed. The first one is the displacement or deflection that the model experiences during the 3D printing process. It is possible to analyze the displacement at a specified timeframe during the printing process. As an example, in Figure 61 the part is presented in both an intermediate and final stage of printing with the same result slider of displacements in mm.

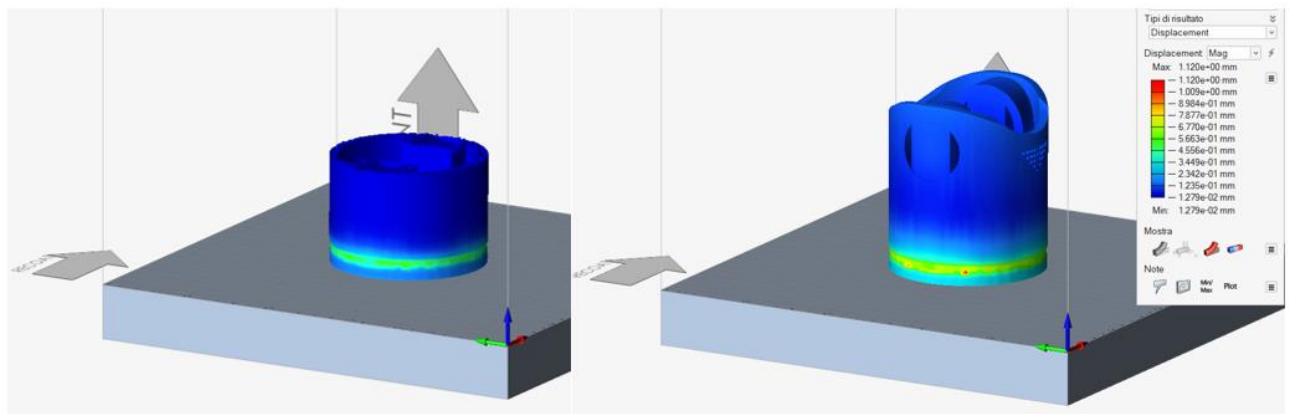


Figure 61 Displacements during the printing phase

The other significant result of this analysis is the temperature of the part. Considering the orientation of the part in the building chamber, the piston top surface is the portion that solidifies first, and this is clear from the left image in Figure 62. Moreover, in the final stage, the sections of the model appear to be at a relatively homogeneous temperature. Figure 62 shows the minimum and maximum value of the temperature of the manufactured part.

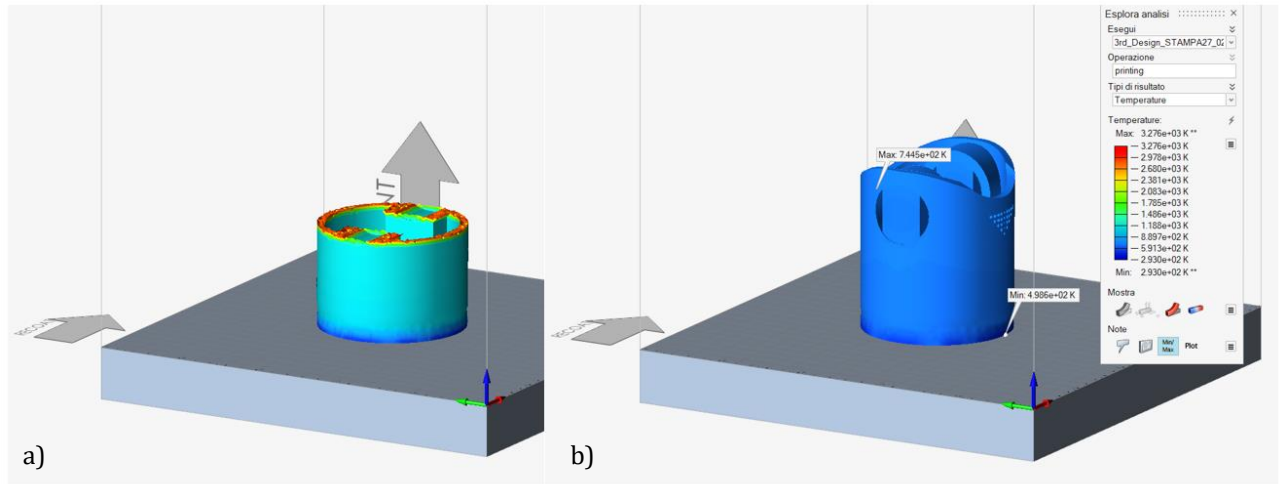


Figure 62 Temperature during printing phase: a) 54.4% and b) 100%

After the build process, the component is not ready to be used and it must undergo significant post-processing. This step is of crucial importance to improve part functionality, dimensional accuracy, mechanical properties and fatigue life of the component. Post-process are out of the scope of the proposed work and will therefore be only briefly described hereafter.

Before removing the part from the platform, a heat treatment is required to relieve residual stresses. The recommended treatment by the EOS systems for AlSi10Mg is a stress-relieving cycle of two hours at 300 °C. During the post-processing, the part is detached from the building plate and the supports are removed. Wire Electrical Discharge Machining (EDM), bandsaws, and/or milling equipment can be used for this purpose. In this case, the realization of the piston ring must be included in the post-processing procedure.

The last step of the SLM process is the surface finishing and it can include abrasive finishing, as polishing and sandpapering, or the application of coatings.

6. Conclusions

Promising additive manufacturing technologies, such as the Selective Laser Melting (SLM) process, mean innovation and this work is in line with this philosophy. The aim of this thesis was to show the advantages, in terms of mass reduction, of re-designing a piston to be produced with optimized process parameters with the AlSi10Mg alloy. Since the performance of SLM parts is affected by many factors rather than a single one, it is extremely interesting to understand how the process variables influence each other and the final mechanical properties. More in detail, this work focuses on the design of the piston starting from its operating conditions moving forward with the steps necessary for its manufacturing with the EOS M290 machine.

The proposed solution of the redesigned component leads to advantages not only in mass reduction (-3%) but also in part quality and material waste if compared to the traditional manufacturing, that is casting for this case. However, the production time of SLM is currently quite high. For this reason, it should be considered that this redesigned component is not ready for batch production and, due to the benefits AM has over traditional manufacturing, this technique could be actively explored for a limited number of components. With the continuous research and development in the AM field, it will be possible to further reduce production time and costs making it competitive with the traditional manufacturing processes.

Appendix

This section reports the complete set of data collected during the density measurements, reported in Table 12, and Vickers hardness in Table 13.

<i>Label</i>	<i>Dry weight 1</i>	<i>Dry weight 2</i>	<i>Wet weight 1</i>	<i>Wet weight 2</i>	<i>Density 1</i>	<i>Density 2</i>	<i>Average density</i>	<i>Relative density</i>	<i>Standard Deviation</i>
<i>l</i>	<i>[g]</i>	<i>[g]</i>	<i>[g]</i>	<i>[g]</i>	<i>[g/cm³]</i>	<i>[g/cm³]</i>	<i>[g/cm³]</i>	<i>[%]</i>	<i>[%]</i>
B	2.56	2.56	1.61	1.60	2.68	2.66	2.67	99.73	1.05
D	2.53	2.53	1.56	1.58	2.65	2.66	2.66	99.07	0.56
F	2.59	2.59	1.62	1.62	2.67	2.67	2.67	99.68	0.17
H	2.57	2.57	1.61	1.61	2.68	2.68	2.68	99.86	0.09
J	2.56	2.56	1.59	1.59	2.65	2.65	2.65	98.87	0.44
L	2.56	2.56	1.60	1.60	2.66	2.65	2.66	99.06	0.24
N	2.60	2.60	1.62	1.62	2.67	2.66	2.66	99.39	0.20
P	2.59	2.59	1.61	1.62	2.66	2.66	2.66	99.29	0.18
Q	2.57	2.57	1.60	1.60	2.65	2.64	2.65	98.79	0.56
R	2.56	2.56	1.60	1.59	2.66	2.66	2.66	99.20	0.21
S	2.58	2.58	1.62	1.61	2.68	2.66	2.67	99.53	0.78
T	2.59	2.59	1.62	1.62	2.67	2.67	2.67	99.63	0.03

Table 12 Complete density measurements

<i>Sample</i>	<i>HV 1</i>	<i>HV 2</i>	<i>HV 3</i>	<i>HV 4</i>	<i>HV 5</i>	<i>HV avg.</i>	<i>Standard deviation</i>
B	126	124	119	123	122	122.8	2.32
D	126	131	129	123	125	126.8	2.86
F	126	130	129	127	126	127.6	1.63
H	127	141	127	126	129	130	5.59
J	120	123	124	121	120	121.6	1.63
L	123	74	124	122	122	113	19.51
N	130	125	125	128	126	126.8	1.94
P	128	123	126	124	126	125.4	1.74
Q	124	128	128	127	127	126.8	1.47
R	129	130	125	126	119	125.8	3.87
S	128	124	135	130	132	129.8	3.71
T	128	135	134	128	133	131.6	3.01

Table 13 Complete Vickers hardness measurements

Among the values in Table 13, the second measurement for the specimen L results to be extremely lower than the others. A reason that can explain this result is that it corresponds to an indentation made on or near a defect of the specimen. For a better understanding of the situation, the hardness values of Table 13 are reported in a boxplot graph in Figure 63.

The boxplot used draws points as outliers if they are greater than (7) or lower than (8).

$$q_3 + w \cdot (q_3 - q_1) \quad (7)$$

$$q_3 - w \cdot (q_3 - q_1) \quad (8)$$

Where w is the multiplier Whisker, and q_1 and q_3 are the 25th and 75th percentiles of the sample data, respectively. In this case study, the Whisker is chosen with a value of 1.75.

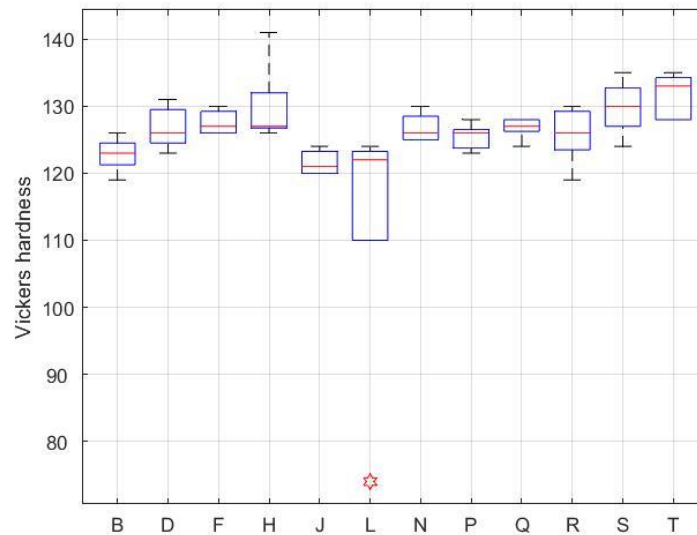


Figure 63 Hardness boxplots

From the plot in Figure 63 is evident that the second measurement of the sample L is an outlier and for this reason it is excluded from the average hardness computation. The average value of 113 for sample L reported in Table 13 is then replaced with 122.75, calculated net of defective measurement. All the plots presented in section 3.3.2 are based on the data set without the outlier.

References

- [1] I. Bhavi, V. V. Kuppast and D. D. Chillal, "Experimental Investigation of Influence of Piston Pin-Offset on Reduction of Piston Slap Noise," *Journal of Failure Analysis and Prevention volume*, 2021.
- [2] L. D. Sturm, C. B. Williams, J. A. Camelio, J. White and R. Parker, "Cyber-physical vulnerabilities in additive manufacturing systems: A case study attack on the .STL file with human subjects," *The Journal of Manufacturing Systems*, 2017.
- [3] C. Y. Yap, C. K. Chua, Z. L. Dong, Z. H. Liu, D. Q. Zhang, L. Loh and S. L. Sing, "Review of selective laser melting: Materials and applications," *Applied Physics Reviews*, 2015.
- [4] M. A. Pekok, R. Setchi, M. Ryan, Q. Han and D. Gu, "Effect of process parameters on the microstructure and mechanical properties of AA2024 fabricated using selective laser melting," *The International Journal of Advanced Manufacturing Technology*, 2021.
- [5] T. Massalski, H. Okamoto, P. Subramanian and L. Kacprzak, *Binary Alloy Phase Diagrams*, 2nd Edition, 1990.
- [6] *Standard Test Methods for Flow Rate of Metal Powders Using the Hall Flowmeter Funnel*, B213-13 ASTM - International, 2013.
- [7] *Standard Test Method for Apparent Density of Free-Flowing Metal Powders Using the Hall Flowmeter Funnel*, B213-21 ASTM- International, 2021.
- [8] *Standard Test Method for Sieve Analysis of Metal Powders*, B214-22 ASTM - International, 2022.
- [9] M. Balbaa, A. Ghasemi, E. Fereiduni, M. Elbestawi, S. Jadhav e J.-P. Kruth, «Role of powder particle size on laser powder bed fusion processability of AlSi10Mg alloy,» *Additive Manufacturing*, vol. 37, 2021.
- [10] M. Saunders, "X marks the spot - find the ideal process parameters for your metal AM parts," *Renishaw plc*, 2019.
- [11] K. Kempen, L. Thijs, E. Yasa and M. Badrossamay, "Process Optimization and Microstructural Analysis for Selective Laser Melting of AlSi10Mg," in *Solid Freeform Fabrication Symposium*, Texas, USA, 2011.

- [12] A. H. Maamoun, Y. F. Xue, M. A. Elbestawi and S. C. Veldhuis, "Effect of Selective Laser Melting Process Parameters on the Quality of Al Alloy Parts: Powder Characterization, Density, Surface Roughness, and Dimensional Accuracy," *Materials*, 2018.
- [13] *Standard Test Methods for Density of Compacted or Sintered Powder Metallurgy (PM) Products Using Archimedes' Principle*, B962-17 ASTM - International, 2017.
- [14] D. Buchbinder, H. Schleifenbaum, S. Heidrich, W. Meiners and J. Bültmann, "High Power Selective Laser Melting (HP SLM) of Aluminum Parts," *Physics Procedia*, 2011.
- [15] E. Olakanmi, R. Cochrane and K. Dalgarno, "A review on selective laser sintering/melting (SLS/SLM) of aluminium alloy powders: Processing, microstructure, and properties," *Progress in Materials Science*, 2015.
- [16] *Standard Test Methods for Vickers Hardness and Knoop Hardness of Metallic Materials*, E92-17 ASTM - International, 2017 .
- [17] J. R. Davis, *ASM Specialty Handbook: Aluminum and Aluminum Alloys*, ASM International , 1993.
- [18] A. H. Maamoun, Y. F. Xue, M. A. Elbestawi and S. C. Veldhuis, "The Effect of Selective Laser Melting Process Parameters on the Microstructure and Mechanical Properties of Al6061 and AlSi10Mg Alloys," *Materials 2019*, 2018.
- [19] T. DebRoy, H. Wei, J. Zuback, T. Mukherjee, J. Elmer, J. Milewski, A. Beese, A. Wilson-Heid, A. De and W. Zhang, "Additive manufacturing of metallic components – Process, structure and properties," *Progress in Materials Science*, 2018.
- [20] M. Tang, "Inclusions, Porosity, and Fatigue of AlSi10Mg Parts Produced by Selective Laser Melting," Pittsburgh, PA, 2017.
- [21] M. Krishnan, E. Atzeni, R. Canali, F. Calignano, D. Manfredi, E. P. Ambrosio and L. Iuliano, "On the effect of process parameters on properties of AlSi10Mg parts produced by DMLS," *Rapid Prototyping Journal*, 2013.
- [22] *Standard Test Methods for Tension Testing of Metallic Materials*, E8/E8M-13a ASTM - International, 2013.
- [23] EOS GmbH - Electro Optical Systems, *Material data sheet - EOS Aluminium AlSi10Mg*, Krailing, München .

